Heliyon 10 (2024) e34614

Contents lists available at ScienceDirect

Heliyon

journal homepage: www.cell.com/heliyon

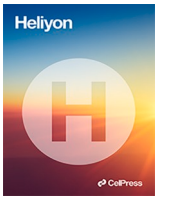

Research article

# Novel nickel-immobilized-$SiO_2$-$TiO_2$ fine particles in the presence of cetyltrimethylammonium bromide as a catalyst for ultrasound-assisted-Kumada cross-coupling reaction

Dewi Agustiningsih [a,b], Eko Sri Kunarti [a,*], Nuryono Nuryono [a], Sri Juari Santosa [a], Muhammad Idham Darussalam Mardjan [a], Yuichi Kamiya [c,**], Ryoichi Otomo [c]

[a] Department of Chemistry, Faculty of Mathematics and Natural Sciences, Universitas Gadjah Mada, Sekip Utara, Yogyakarta, 55281, Indonesia
[b] Graduate School of Environmental Science, Hokkaido University, Nishi 5, Kita 10, Kita-ku, Sapporo, 060–0810, Japan
[c] Faculty of Environmental Earth Science, Hokkaido University, Nishi 5, Kita 10, Kita-ku, Sapporo, 060–0810, Japan

ARTICLE INFO

*Keywords:*
Silica-titania
Cetyltrimethylammonium bromide
Nickel
Kumada cross-coupling reaction
Sonication

ABSTRACT

Kumada cross-coupling reaction is useful for producing biphenyls, where nickel and copper have been widely investigated as catalysts but mainly homogeneous ones. In this study, we investigated ultrasound-assisted-Kumada cross-coupling reaction over the heterogeneous catalysts in which $Ni^{2+}$, $Cu^{2+}$, or both was immobilized on aminopropylsilane-functionalized-$SiO_2$-$TiO_2$ prepared in the presence of cetyltrimethylammonium bromide (CTAB). The presence of CTAB effectively prevented the particle growth and therefore $SiO_2$–$TiO_2$ fine particles with high surface area (502 $m^2$ $g^{-1}$) were formed. The $Ni^{2+}$-immobilized catalyst showed high catalytic activity for the ultrasound-assisted-Kumada cross-coupling reaction of a wide variety of substrates and was reusable three times. Performing the reaction under ultrasound irradiation was very effective in significantly accelerating the reaction rate compared with the conventional mechanical method. In contrast to $Ni^{2+}$, $Cu^{2+}$ was deposited on the support as crystalline $Cu(OH)_2$ and the resulting catalysts with $Cu^{2+}$ and $Ni^{2+}$-$Cu^{2+}$ were less active and less stable under the reaction conditions.

## 1. Introduction

Over the years, the utilization of metal and metal ions as an active center of catalysts in organic reactions has gained widespread attention. Notably, noble metals such as Pt and Pd have been demonstrated to show very high activity in various organic reactions such as oxidation [1,2], reduction [3,4], cross-coupling [5–7], and isomerization [8,9]. Despite their high catalytic activity, noble metals have a critical problem of being overpriced mainly due to scarcity and burdensome refining. Thus, the use of more abundant and cost-effective non-noble metals has been intensively investigated [10]. Among such metals, nickel is one of the most interesting ones due to its advantageous activity for many organic reactions [10,11] specifically cross-coupling reactions for C–C bond formation [12,13], whose activity is almost equivalent to, and in some reactions, exceeds the activities of noble metals. In addition, copper also has significant attention owing to its ease of availability and low cost, while the application of copper as a catalyst has been less extensive than nickel [14–17].

* Corresponding author.
** Corresponding author.
*E-mail addresses:* eko_kunarti@ugm.ac.id (E.S. Kunarti), kamiya@ees.hokudai.ac.jp (Y. Kamiya).

https://doi.org/10.1016/j.heliyon.2024.e34614
Received 12 April 2024; Received in revised form 19 May 2024; Accepted 12 July 2024
Available online 14 July 2024

Homogeneous catalysts are useful due to high catalytic performance but have inherent drawbacks such as low thermal stability and difficulty of separation from the reaction solution, causing potential contamination of the final product with the metal components, which is a critical issue, especially in the synthesis of pharmaceutical intermediates. On the other hand, heterogeneous catalysts with metals and metal ions have excellent properties, including high thermal stability, ease of separation, and high reusability, which homogenous ones do not have. Among support materials for such heterogeneous catalysts, silica is one of the most common due to its high surface area [18], controlled particle and pore sizes [19], decent thermal stability [20], ease of preparation, and so on [21]. Nonetheless, silica has a crucial limitation as a support material, that is its weak interaction with metals and metal ions, which potentially causes leaching and aggregation of the active metals and metal ions species during reactions. One approach to solve this problem is to combine silica with other materials such as titania. Since titania can strongly interact with metals and metal ions [22–24], mixing silica with titania will give an excellent support material with a high ability to immobilize metals and metal ions, while maintaining the excellent characteristics of silica. In fact, Viéitez-Calo et al. demonstrated the efficacy of $SiO_2$–$TiO_2$ composite as a support material for Pt catalyst [25]. Their findings underscored a synergistic benefit of this combination, where $TiO_2$ brought strong interaction with Pt, which prevented the aggregation of Pt particles, while $SiO_2$ contributed to high surface area and thermal stability.

In our previous study [26], we developed a heterogeneous nickel catalyst where $Ni^{2+}$ was immobilized on (3-aminopropyl)triethoxysilane-functionalized $SiO_2$–$TiO_2$ composite ($SiO_2$–$TiO_2$@APTES). The use of APTES as a linker agent has been widely studied owing to the bifunction derived from ethoxysilane and amino group [17,27–39]. Ethoxysilane in APTES is used to fix it on a support material, while the amino group is projected to strongly bind $Ni^{2+}$ through a coordination bond. Hence, $Ni^{2+}$ was immobilized on the surface of $SiO_2$–$TiO_2$@APTES not only through relatively weak interaction with silanol and titanol but also through strong interaction with amino groups [26]. This catalyst exhibited high catalytic activity for Kumada cross-coupling reaction to produce biphenyls [26], which are important intermediates in the pharmaceutical and agrochemical sectors [40,41]. Kumada cross-coupling reaction was first demonstrated in 1972 by Kumada et al. with the use of nickel(II) complexes as homogenous catalyst [12]. In addition, some transition metal complexes other than nickel were also used in homogeneous catalysts for Kumada cross-coupling reaction, including palladium [42,43], iron [44,45], copper [15,46], cobalt [47–49], manganese [50], and chromium [51].

Based on our previous study, the present study addressed the following three aspects. The first aspect was the preparation of $SiO_2$–$TiO_2$ composites using cetyltrimethylammonium bromide (CTAB) as a particle growth inhibitor. In our previous study [26], polyethylene glycol (PEG) was used as a particle growth inhibitor, but the inhibition effect of PEG was not so strong that agglomeration of $SiO_2$–$TiO_2$ particles was not suppressed so much, resulting in the formation of large particles (about 300 nm). Meanwhile, CTAB is an amphiphilic molecule with a long alkyl chain and is known to show a strong inhibition effect. In fact, Rana [52], Ismail et al. [53], and Yadav et al. [54] successfully prepared fine particles (less than 100 nm) of ZnO, α-$Ag_2S$, and NiO, respectively, with high surface areas.

The second aspect was performing the ultrasound-assisted-Kumada cross-coupling reaction using our catalyst. In our previous study [26], conventional mechanical mixing with a magnetic stirrer was employed for the reaction. In this study, the mixing of the reaction solution by sonication was investigated. The advantages of sonication-mixing are to make reaction conditions mild, that is, low reaction temperature and short reaction time [55], which are caused by an acoustic cavitation effect in the formation [56], growth, and implosion of bubbles [57]. In fact, the sonication-mixing is widely applied for organic reactions, particularly for cross-coupling reactions such as Heck, Hiyama [58], Chan-Lam, Stille [59], and Suzuki-Miyaura reactions [33,60–63], while to the best of our knowledge, there is no report on Kumada cross-coupling reaction under ultrasound irradiation.

The third aspect addressed in this study was the application of $Cu^{2+}$ as an active center of the catalyst immobilized on $SiO_2$–$TiO_2$@APTES. Copper catalysts often have high activity in some cross-coupling reactions including Suzuki-Miyaura [64], Sonogashira [65], and Chan-Lam [66] reactions, while are used as a homogeneous catalyst in many cases. Thus, we attempted to immobilize $Cu^{2+}$ on $SiO_2$–$TiO_2$@APTES and applied it for an ultrasound-assisted-Kumada cross-coupling reaction.

## 2. Experimental section

### 2.1. Preparation of $SiO_2$–$TiO_2$ composite

$SiO_2$–$TiO_2$ composite was prepared using a sol-gel method in the presence of CTAB. Initially, 2.9 g (0.007 mol) of CTAB (98 %, FUJIFILM Wako Pure Chemical Co.) was dissolved in 29 mL of aqueous ammonia (0.512 mol $L^{-1}$). The mixture was stirred at 40 °C until complete dissolution of CTAB. Subsequently, 1.645 mL (0.007 mol) of tetraethyl orthosilicate (TEOS, 95 %, FUJIFILM Wako Pure Chemical Co.), which was dissolved in 16 mL of ethanol (99.5 %, FUJIFILM Wako Pure Chemical Co.), was added to the CTAB solution, and the mixture was stirred at 40 °C for 1 h to form silica sol. The obtained sol was then allowed to stand for 12 h and silica gel was formed [67].

Next, 2.1 mL (0.007 mol) of titanium tetraisopropoxide (95 %, FUJIFILM Wako Pure Chemical Co.), which was dissolved in 21 mL of ethanol, was added to the resulting silica gel, and the mixture was sonicated for 3 h and then stirred for 4 h at room temperature. After it was allowed to stand for 12 h, the resulting gel was collected by filtration and washed with Milli-Q water. After drying at 60 °C for 12 h, the solid was calcined at 600 °C for 3 h in air flow (10 mL $min^{-1}$). The resulting solid ($SiO_2$–$TiO_2$ composite) is denoted as $ST_1$, where S and T mean $SiO_2$ and $TiO_2$, respectively, and 1 is a molar ratio of CTAB to $SiO_2$–$TiO_2$. $ST_n$ ($n$ = 0.1–1.2) was also prepared similarly to that for $ST_1$ but the amount of CTAB was different [24,26].

### 2.2. Functionalization of $ST_1$ with (3-aminopropyl)triethoxysilane (APTES)

While details will be given later in Results and Discussion, $ST_1$ was the most suitable support material among $ST_n$. Therefore, $ST_1$

was further modified with APTES as follows. Firstly, 1 g of APTES (98 %, FUJIFILM Wako Pure Chemical Co.) was dissolved in 10 mL of ethanol (99.5 %, FUJIFILM Wako Pure Chemical Co.) and the mixture was stirred at room temperature for 15 min. Separately, 1 g of $ST_1$ was dispersed in 10 mL of ethanol. The APTES solution was then added to the $ST_1$ suspension, and the mixture was sonicated for 2 h and stirred for 6 h at room temperature. The resulting solid was collected by filtration, washed with ethanol and Milli-Q water three times each, and then dried at 60 °C for 12 h. The resulting solid was denoted as $ST_1N$ [24,26].

### 2.3. Immobilization of $Ni^{2+}$, $Cu^{2+}$, and $Ni^{2+}$-$Cu^{2+}$ onto $ST_1N$

One gram of $ST_1N$ was dispersed in 10 mL of Milli-Q water. Concurrently, an aqueous $Ni^{2+}$ solution was prepared by dissolving 0.7130 g (3 mmol) of $NiCl_2{\cdot}6H_2O$ (FUJIFILM Wako Pure Chemical Co.) in 10 mL of Milli-Q water. The $Ni^{2+}$ solution was transferred to the $ST_1N$ suspension, and the mixture was stirred at room temperature. After 24 h, the solid was collected by filtration, washed with Milli-Q water three times, and dried at 60 °C for 12 h. The obtained solid was denoted as $ST_1N/Ni_3$, where 3 was $Ni^{2+}$ dose (mmol) to 1 g of $ST_1N$, i.e., 3 mmol/g. It is noted that the actual $Ni^{2+}$ amount immobilized on $ST_1N/Ni_3$ was less than the dose and will be shown in detail later. Similarly, $ST_1N/Ni_5$, $ST_1N/Ni_7$, and $ST_1N/Ni_{10}$ were prepared.

The immobilization of $Cu^{2+}$ on $ST_1N$ was performed in a similar manner to that for $ST_1N/Ni_x$ but employing $CuCl_2{\cdot}2H_2O$ (FUJIFILM Wako Pure Chemical Co.) instead of $NiCl_2{\cdot}6H_2O$. Bimetallic $Ni^{2+}$-$Cu^{2+}$ catalysts were also prepared using a solution containing both $NiCl_2{\cdot}6H_2O$ and $CuCl_2{\cdot}2H_2O$. $Ni^{2+}/Cu^{2+}$ molar ratios were varied as 0.5, 1, and 2 keeping the total dose at 10 mmol, and the obtained solids were denoted as $ST_1N/NiCu_2$, $ST_1N/NiCu$, and $ST_1N/Ni_2Cu$, respectively [24,26].

### 2.4. Characterization

Measurement of powder X-ray diffraction (XRD) pattern was performed using a D2 PHASER 2nd Generation XRD (Bruker) with Cu Kα radiation. Attenuated total reflectance infrared spectroscopy (IR) measurement was carried out on a NICOLET iS10 PIKE GladiATR (Thermo Scientific). Nitrogen adsorption-desorption isotherms were taken on a Belsorp mini instrument (BEL Japan) at −196 °C. Before the measurement, samples were treated in $N_2$ flow (25 mL $min^{-1}$) at 150 °C for 1 h. The obtained isotherm was analyzed by the Brunauer-Emmett-Teller (BET) and Barrett-Joyner-Halenda methods to obtain specific surface area and pore size distribution, respectively. UV–Vis absorbance of each sample was analyzed on a UV–Vis–NIR spectrophotometer (UV-3600 Plus, Shimadzu).

Dynamic light scattering (DLS) analysis was performed on a Zetasizer Pro (MALVERN) to simultaneously determine particle size distribution and zeta potential of the samples. Specimen for the DLS measurement was prepared by dispersing 10 mg of the sample in 50 mL of ethanol-water 3:1 mixture (v/v). Thermogravimetric (TG) profile was measured on a Thermo plus TG 8120 (Rigaku) in the air (50 mL $min^{-1}$) at 10 °C $min^{-1}$. Actual metal loadings of Ni and Cu were determined by using inductively coupled plasma-atomic emission spectroscopy (ICP-AES, ICPE-9000, Shimadzu). For the measurement, the sample was dissolved in $HNO_3$ (65 %, FUJIFILM Wako Pure Chemical Co.) at 80 °C for 6 h, and the solution was diluted with Milli-Q water. The morphology of the samples was observed on a transmission electron microscope (TEM, JEM-2010, JEOL).

The composition of the samples and oxidation state of metal species on the surface was determined by X-ray photoelectron spectroscopy (XPS, JPS-9200, JEOL) with Al Kα radiation. Before the measurement, the samples were pre-treated at 60 °C for 24 h under vacuum. Elemental analysis to determine the contents of carbon and nitrogen was performed using an elemental analyzer (EA, CE440, EAI Exeter Analytical) at the Global Facility Center, Hokkaido University.

### 2.5. Ultrasound-assisted-Kumada cross-coupling reaction

Ultrasound-assisted-Kumada cross-coupling reaction to produce biphenyl compounds was performed to evaluate the catalytic performance. Catalyst powder (50 mg) was added to a mixture of Grignard reagents (RMgX, 1 mmol, 16 % in tetrahydrofuran, Tokyo Chemical Industry), halobenzene (PhX, 1 mmol, 98 %, FUJIFILM Wako Pure Chemical Co.), and 2 mL of tetrahydrofuran (THF, FUJIFILM Wako Pure Chemical Co.) in a test tube with a cap. The mixture in the test tube was sonicated at 50 °C for 90 min using an ultrasonic cleaner (MCS-2, AS ONE Co., single frequency mode). After the reaction, the catalyst powder was separated using a syringe filter (with a pore size of 0.1 μm), and the obtained solution was analyzed by a gas chromatography (GC, GC-2025, Shimadzu) equipped with a flame ionization detector and a capillary column (DB-17, Agilent J&W). The concentrations of unreacted reactants and formed products were determined using tetradecane as an internal standard, and the conversion and yield of biphenyl were calculated by eqs. (1) and (2), respectively.

$$\text{Conversion}\ (\%) = \frac{\text{reacted amount of reactant}}{\text{initial amount of reactant}} \times 100 \tag{1}$$

$$\text{Yield of biphenyl}\ (\%) = \frac{\text{produced amount of biphenyl}}{\text{initial amount of reactant}} \times 100 \tag{2}$$

The reactions with different reaction times, temperatures, and catalyst doses, and those in various solvents including THF, chloroform, dichloromethane, toluene, acetonitrile, and 1,4-dioxane were also performed.

A reusability test of the catalyst was performed. After the reaction, the catalyst was collected by filtration, washed with ethanol and Milli-Q water three times each, dried at 60 °C for 12 h, and then served for the following reaction.

A hot filtration test was also conducted to know whether a reaction took place on the catalyst surface, namely, a heterogeneous

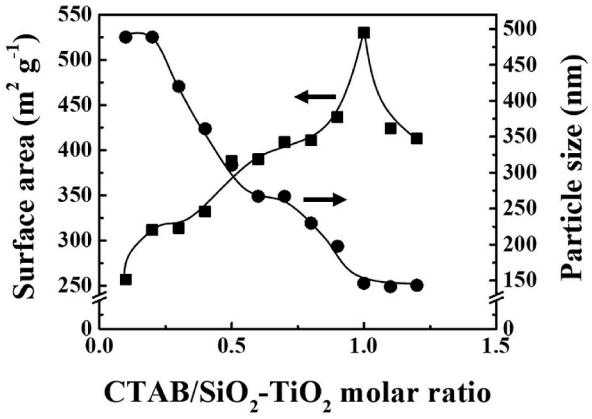


**Fig. 1.** Surface area and average particle size of $ST_n$ prepared with different CTAB amounts.

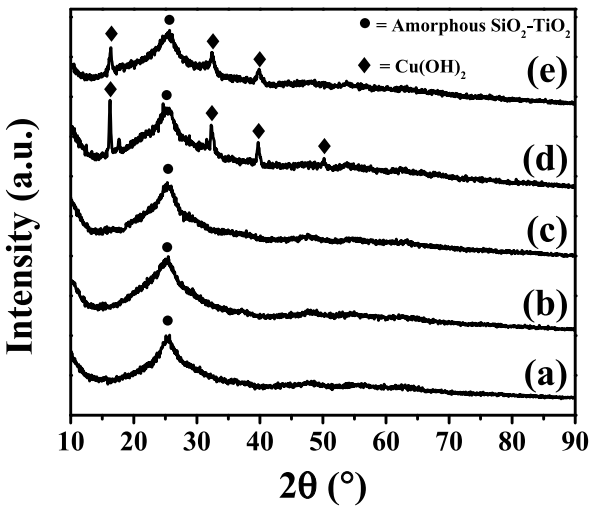


**Fig. 2.** XRD patterns of (a) $ST_1$, (b) $ST_1N$, (c) $ST_1N/Ni_{10}$, (d) $ST_1N/Cu_{10}$, and (e) $ST_1N/Ni_2Cu$.

catalytic reaction. After 30 min from the beginning of the reaction, the solid catalyst was removed from the reaction solution by filtration. Then, the reaction was further continued with the obtained solution up to 120 min, and the reaction solution was analyzed at 45, 60, 75, 90, 105, and 120 min.

Biphenyl contained in the crude product solution was isolated by washing it with Milli-Q water and ethyl acetate (FUJIFILM Wako Pure Chemical Co.). The obtained organic phase was dried with anhydrous $Na_2SO_4$ (FUJIFILM Wako Pure Chemical Co.) and the solvent was then removed using a rotary evaporator (N-1110, EYELA World) at 90 °C for 30 min. A small quantity of white crystal, expected to be solid biphenyl was obtained and was characterized on a proton nuclear magnetic resonance ($^1$H NMR, JMTC-500/53/JJ, JASTEC SUPERCONDUCTOR).

## 3. Results and Discussion

In the preparation of $SiO_2$–$TiO_2$ composites, the amount of CTAB, consequently the CTAB/$SiO_2$–$TiO_2$ ratio, was varied to study the influence of CTAB on crystalline structure, particle size, and surface area of the resulting materials. As shown in Fig. S1, all the $SiO_2$–$TiO_2$ composites were amorphous regardless of the amount of CTAB. In addition, there was no difference in IR spectra of all the $SiO_2$–$TiO_2$ composites (Fig. S2), while no absorption band due to the appearance of CTAB. These results demonstrated that the amount of CTAB did not affect the bulk structure of the $SiO_2$–$TiO_2$ composite.

In contrast, the amount of CTAB had a large impact on particle size and surface area of the $SiO_2$–$TiO_2$ composites. Fig. 1 shows the surface area and average particle size of $ST_n$ prepared with different CTAB amounts. The surface area and average particle size of $ST_{0.1}$ were 257 $m^2$ $g^{-1}$ and 489 nm, respectively, which were almost the same as those of the $SiO_2$–$TiO_2$ composite prepared in the presence of PEG [26]. As expected, the average particle size was monotonically decreased with an increase in the amount of CTAB due to the inhibition effect of CTAB [68–71]. Accordingly, the surface area was increased and $ST_1$ had the largest one among $ST_n$, which was 502

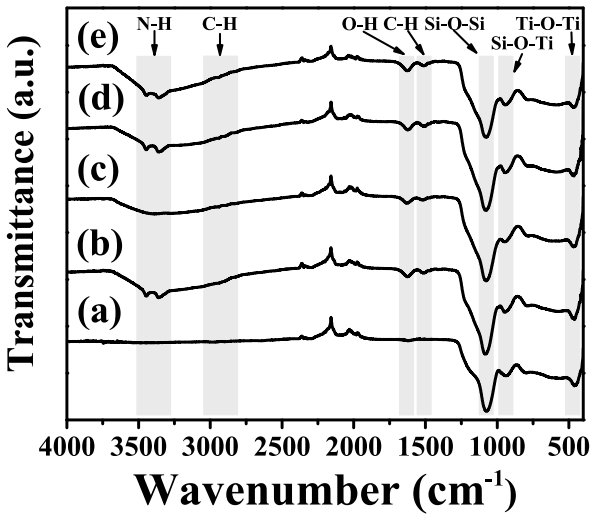


**Fig. 3.** IR spectra of (a) $ST_1$, (b) $ST_1N$, (c) $ST_1N/Ni_{10}$, (d) $ST_1N/Cu_{10}$, and (e) $ST_1N/Ni_2Cu$.

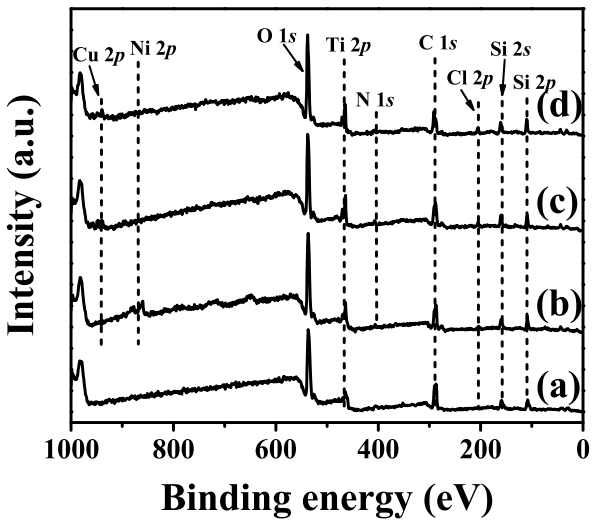


**Fig. 4.** XPS wide scan spectra of (a) $ST_1N$, (b) $ST_1N/Ni_{10}$, (c) $ST_1N/Cu_{10}$, and (d) $ST_1N/Ni_2Cu$.

$m^2\ g^{-1}$. It is noted that $ST_1$ had a significantly large surface area, even though the average particle size of $ST_1$ was almost the same as those of other samples including $ST_{1.1}$ and $ST_{1.2}$. This was due to the presence of well-developed pores inside the particles of $ST_1$. Because of the small particle size and high surface area, we chose $ST_1$ as a support material appropriate for further modification with APTES and subsequent immobilization of $Ni^{2+}$ and $Cu^{2+}$.

Fig. 2 displays XRD patterns of the prepared materials including $ST_1$, $ST_1N$, $ST_1N/Ni_{10}$, $ST_1N/Cu_{10}$, and $ST_1N/Ni_2Cu$. It is evident that the amorphous nature of $ST_1$ was maintained even after the modification with APTES. The introduction of $Ni^{2+}$ to $ST_1N$ did not give any crystalline nickel compounds like NiO and $Ni(OH)_2$, implying that $Ni^{2+}$ was highly dispersed in $ST_1N/Ni_{10}$. In contrast, distinct diffraction lines assigned to crystalline $Cu(OH)_2$ (JCPDS No 13–420, [72,73]) appeared with the introduction of $Cu^{2+}$. For $ST_1N/Ni_2Cu$, in which both $Ni^{2+}$ and $Cu^{2+}$ were introduced, sharp diffraction lines due to $Cu(OH)_2$ were also observed, but no diffraction line attributable to crystalline Ni compounds appeared. A possible reason for the difference in the existing states between Ni and Cu species on the corresponding materials was the difference in the solubility of the respective hydroxides. The solubility of $Cu(OH)_2$ ($K_{sp} = 2.2 \times 10^{-20}$ at 25 °C) is four orders of magnitude lower than that of $Ni(OH)_2$ ($K_{sp} = 1.6 \times 10^{-16}$ at 25 °C), meaning that $Cu^{2+}$ is more easily precipitated than $Ni^{2+}$. To investigate the difference in the formation behavior of the hydroxides, the pH of the solutions of $NiCl_2{\cdot}6H_2O$ and $CuCl_2{\cdot}6H_2O$ were changed by the addition of an aqueous NaOH solution, and the changes in the appearance of the solutions were observed. pH of the solutions of $NiCl_2{\cdot}6H_2O$ and $CuCl_2{\cdot}6H_2O$ immediately after preparation were 5.1 and 3.2, respectively, and both solutions were transparent (Fig. S3). The aqueous NaOH solution was added to the solutions of $NiCl_2{\cdot}6H_2O$ and $CuCl_2{\cdot}6H_2O$ and when the pH reached 6.7 and 3.5, respectively, the corresponding hydroxides were formed (Fig. S3).

**Table 1**
XPS atomic composition of the prepared materials calculated from narrow scan spectra.

| Materials | Atomic composition (%) | | | | |
|---|---|---|---|---|---|
| | O1*s* | N1*s* | C1*s* | Ni2$p_{3/2}$ | Cu2$p_{3/2}$ |
| $ST_1N$ | 48.34 | 2.73 | 48.93 | – | – |
| $ST_1N/Ni_{10}$ | 55.93 | 2.68 | 39.55 | 1.84 | – |
| $ST_1N/Cu_{10}$ | 48.84 | 2.55 | 47.16 | – | 1.45 |
| $ST_1N/Ni_2Cu$ | 50.75 | 2.10 | 45.36 | 0.43 | 1.36 |

**Table 2**
Surface area and average pore diameter of the samples.

| Samples | Surface area[a] ($m^2\ g^{-1}$) | Average pore diameter[b] (nm) |
|---|---|---|
| $ST_1$ | 502 | 5 |
| $ST_1N$ | 172 | 8 |
| $ST_1N/Ni_{10}$ | 222 | 6 |
| $ST_1N/Cu_{10}$ | 94 | 10 |
| $ST_1N/Ni_2Cu$ | 123 | 9 |

[a] BET surface area.
[b] Determined based on BJH theory.

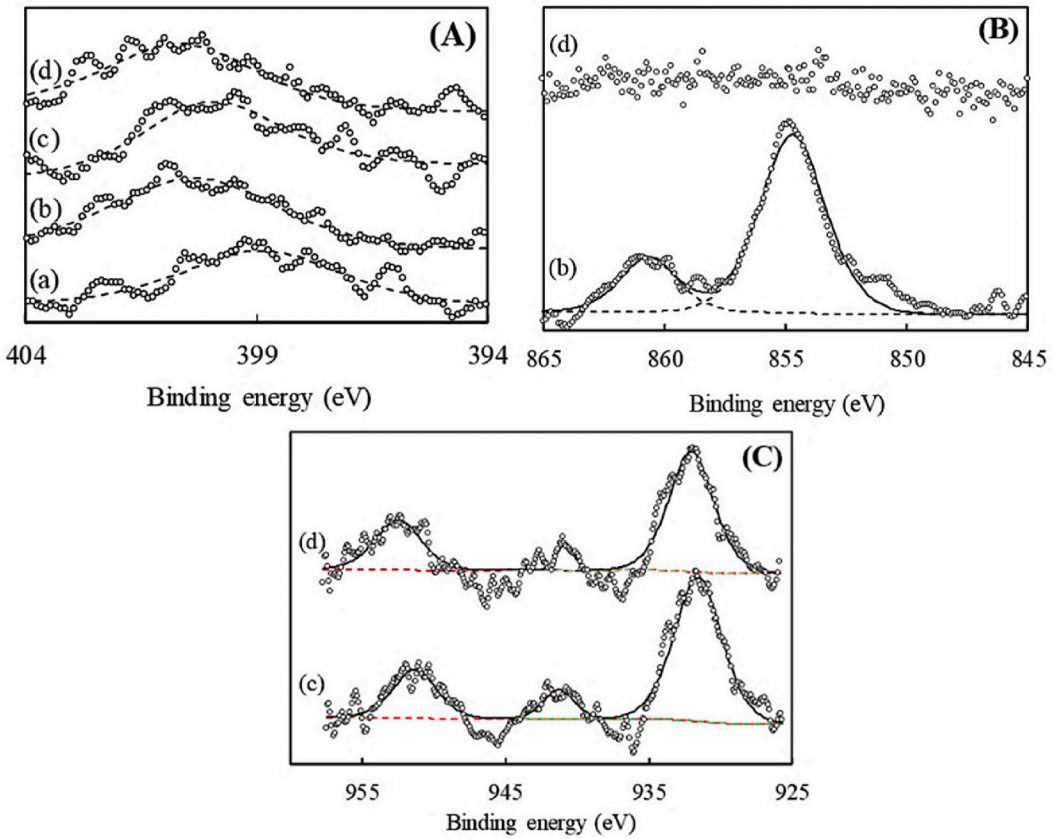


**Fig. 5.** (A) N 1s, (B) Ni 2p, and (C) Cu 2p XPS narrow spectra of (a) $ST_1N$, (b) $ST_1N/Ni_{10}$, (c) $ST_1N/Cu_{10}$, and (d) $ST_1N/Ni_2Cu$.

This fact certainly reflected the difference in the solubilities of $Ni(OH)_2$ and $Cu(OH)_2$. Since $ST_1N$ had amino groups on the surface, the pH of the solutions of $NiCl_2{\cdot}6H_2O$ and $CuCl_2{\cdot}6H_2O$ should go up when $ST_1N$ was added to the solutions. As was confirmed experimentally, even a slight increase in the pH of the solution produced the hydroxide for $Cu^{2+}$. Hence, $Cu^{2+}$ was not highly dispersed but was immobilized as $Cu(OH)_2$ in $ST_1N/Cu_{10}$ and $ST_1N/Ni_2Cu$.

Fig. 3 show IR spectra of $ST_1$, $ST_1N$, $ST_1N/Ni_{10}$, $ST_1N/Cu_{10}$, and $ST_1N/Ni_2Cu$. In $ST_1$, the presence of $SiO_2$–$TiO_2$ is confirmed by the

**Table 3**
Dose, actual amount, and actual ratio of $Ni^{2+}/Cu^{2+}$ in $ST_1N/Ni_xCu_y$.

| Sample | Dose[a] (mmol/g) | | Actual[b] (mmol/g) | | Actual $Ni^{2+}/Cu^{2+}$ ratio |
|---|---|---|---|---|---|
| | $Ni^{2+}$ | $Cu^{2+}$ | $Ni^{2+}$ | $Cu^{2+}$ | |
| $ST_1N/NiCu_2$ | 3.3 | 6.7 | 1.5 | 3.0 | 0.50 |
| $ST_1N/NiCu$ | 5.0 | 5.0 | 1.5 | 2.9 | 0.52 |
| $ST_1N/Ni_2Cu$ | 6.7 | 3.3 | 1.5 | 2.7 | 0.56 |

[a] Initial amount added during catalyst preparation.
[b] Determined by ICP-AES.

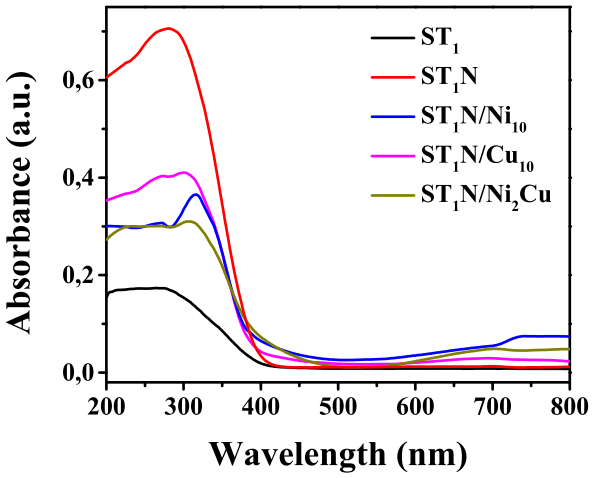


**Fig. 6.** Solid UV–Vis absorption spectra of $ST_1$, $ST_1N$, $ST_1N/Ni_{10}$, $ST_1N/Cu_{10}$, and $ST_1N/Ni_2Cu$.

peaks at 1070, 940, and 460 $cm^{-1}$ which correspond to Si–O–Si stretching, Si–O–Ti stretching, and Ti–O–Ti stretching [74], respectively. After the modification of $ST_1$ with APTES, several new bands due to APTES appeared at around 3400, 2900, and 1470 $cm^{-1}$ for N–H stretching, $C(sp^3)$-H stretching, and $–CH_2$- bending, respectively, demonstrating successful introduction of APTES. With the introduction of $Ni^{2+}$, the bands of N–H stretching disappeared in $ST_1N/Ni_{10}$, while $ST_1N/Ni_{10}$ had C and N of 3.58 and 1.06 wt%, which corresponded to 2.98 and 0.76 mmol/g, respectively. This disappearance of the N–H stretching bands suggested the formation of the coordination bond between the amino group and $Ni^{2+}$ in $ST_1N/Ni_{10}$ [26]. In contrast, on the IR spectra of $ST_1N/Cu_{10}$ and $ST_1N/Ni_2Cu$, the bands of N–H stretching remained. This was consistent with the formation of $Cu(OH)_2$ in these materials. In $ST_1N/Ni_2Cu$, it would seem that $Ni^{2+}$ could be fixed on the amino group, resulting in the disappearance of the bands of N–H, but this did not happen. This was probably due to that $Cu(OH)_2$ was formed first on the surface of $ST_1N$, which prevented $Ni^{2+}$ from getting close to the amino group.

Fig. 4 depicts XPS wide scan spectra of $ST_1N$, $ST_1N/Ni_{10}$, $ST_1N/Cu_{10}$, and $ST_1N/Ni_2Cu$. The spectra reveal peaks corresponding to all elements present in the material, including Si (109.1 and 157.3 eV), Ti (466.2 eV), O (537.1 eV), C (289.2 eV), and N (398.9 eV). Notably, the introduction of metal ions was confirmed by Ni 2p peaks between 850 and 860 eV and Cu 2p peaks between 925 and 955 eV. A peak attributed to Cl at 289.2 eV indicates the presence of chloride originating from metal ion precursors as anion for $Ni^{2+}$ and $Cu^{2+}$. In addition, we also calculated the atomic composition of each sample based on the narrow scan spectra of O 1s, N 1s, C 1s, Ni $2p_{3/2}$, and Cu $2p_{3/2}$ as listed in Table 1.

Fig. 5 shows N 1s, Ni 2p, and Cu 2p XPS narrow spectra of $ST_1N$, $ST_1N/Ni_{10}$, $ST_1N/Cu_{10}$, and $ST_1N/Ni_2Cu$, which were calibrated using C 1s peaks. The N 1s spectrum of $ST_1N$ displayed a peak at 398.9 eV, which was assigned to the amino group in the sample [75] and the peak was slightly shifted to the high binding energy side with the introduction of $Ni^{2+}$ (Fig. 5A). $ST_1N/Cu_{10}$ and $ST_1N/Ni_2Cu$ gave the peaks at 400.0 and 400.1 eV, respectively, on the N 1s spectra (Fig. 5A), and those binding energies were almost the same as that for $ST_1N/Ni_{10}$. On the Ni 2p spectrum of $ST_1N/Ni_{10}$ (Fig. 5B), two peaks attributed to $Ni^{2+}$ were observed at 860.9 (Ni $2p_{1/2}$) and 854.7 eV (Ni $2p_{3/2}$). In contrast, $ST_1N/Ni_2Cu$ did not give any peaks on the Ni 2p spectrum. As will be discussed later, $ST_1N/Ni_2Cu$ did indeed contain Ni, which was confirmed by ICP-AES (Table 3), and thus $Ni^{2+}$ was thought to be buried in the $Cu(OH)_2$ particles. The peaks corresponding to $Cu^{2+}$ were observed for both $ST_1N/Cu_{10}$ and $ST_1N/Ni_2Cu$ (Fig. 5C). There was no significant difference in the Cu 2p spectra between $ST_1N/Cu_{10}$ and $ST_1N/Ni_2Cu$, which is consistent with that $Cu^{2+}$ was immobilized as crystalline $Cu(OH)_2$ in both samples.

Fig. 6 depicts the Solid UV–Vis absorption spectra of the prepared materials including $ST_1$, $ST_1N$, $ST_1N/Ni_{10}$, $ST_1N/Cu_{10}$, and $ST_1N/Ni_2Cu$. The spectra of $ST_1$ exhibits an absorption band at a wavelength below 300 nm, which is characteristic of the $SiO_2$–$TiO_2$ composite [76]. After the functionalization with APTES, a new band with high intensity appeared at 280 nm corresponding to the

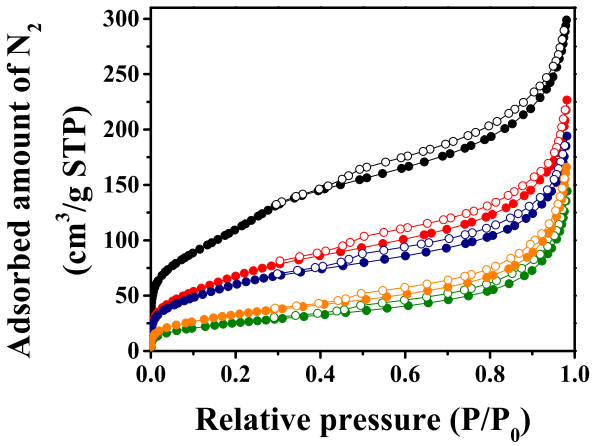


**Fig. 7.** $N_2$ adsorption-desorption isotherms of (●,○) $ST_1$, (●,○) $ST_1N$, (●,○) $ST_1N/Ni_{10}$, (●,○) $ST_1N/Cu_{10}$, and (●,○) $ST_1N/Ni_2Cu$. Closed and open symbols are adsorption and desorption branches, respectively.

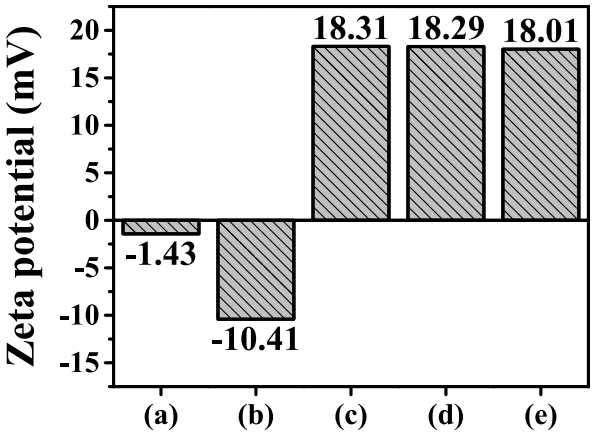


**Fig. 8.** Zeta potential of (a) $ST_1$, (b) $ST_1N$, (c) $ST_1N/Ni_{10}$, (d) $ST_1N/Cu_{10}$, and (e) $ST_1N/Ni_2Cu$.

electron transition in the amine group of APTES, specifically n→σ* on the N–H bond. The band shifted to a higher wavelength (redshift) after $Ni^{2+}$ was introduced, signifying a weakening of the N–H bond strength due to the formation of a coordination bond between $Ni^{2+}$ and the amino group [77]. However, the shift is less pronounced in $ST_1N/Cu_{10}$ and $ST_1N/Ni_2Cu$ due to the presence of $Cu(OH)_2$ failing to form a coordination bond with the amino group.

Fig. 7 illustrates $N_2$ adsorption-desorption isotherms for $ST_1$, $ST_1N$, $ST_1N/Ni_{10}$, $ST_1N/Cu_{10}$, and $ST_1N/Ni_2Cu$, and Table 2 lists the surface area and average pore diameter of the samples. $ST_1$ had a very high surface area of 502 $m^2\ g^{-1}$ and small pores whose average diameter was 5 nm. As has been discussed before, the high surface area of $ST_1$ was brought about by the strong inhibition effect of CTAB on particle growth. The modification of $ST_1$ with APTES to give $ST_1N$ significantly decreased the surface area. This decrease was due to the particle agglomeration caused by strong attraction between amino groups in the different particles or by the progression of condensation of silanol and titanol on $ST_1$ during the modification with APTES. The surface area was increased after the introduction of $Ni^{2+}$, which was due to the removal of unreacted APTES blocking the pores or the weakening of the attraction between the amino groups by the presence of $Ni^{2+}$ on the amino group. The introduction of $Cu^{2+}$ and co-introduction of $Cu^{2+}$ and $Ni^{2+}$ resulted in a significant decrease in the surface area, and this was due to the pore blocking by the $Cu(OH)_2$ particles.

Fig. 8 illustrates zeta potential values of $ST_1$, $ST_1N$, $ST_1N/Ni_{10}$, $ST_1N/Cu_{10}$, and $ST_1N/Ni_2Cu$. $ST_1$ had a little negative value of zeta potential due to the presence of silanol and titanol groups. The modification of $ST_1$ with APTES gave $ST_1N$ enhanced negative zeta potential because APTES having a basic amino group was present on the surface. The subsequent introduction of $Ni^{2+}$, $Cu^{2+}$, and both, conversely, made zeta potential positive, supporting the presence of these metal ions in $ST_1N/Ni_{10}$, $ST_1N/Cu_{10}$, and $ST_1N/Ni_2Cu$.

Fig. 9 shows TEM images of $ST_1$, $ST_1N$, $ST_1N/Ni_{10}$, $ST_1N/Cu_{10}$, and $ST_1N/Ni_2Cu$. As Fig. 9a shows, $ST_1$ was a spherical-shaped particle. After the modification with APTES, an indistinct thin layer with a brighter color was observed over the particle, which

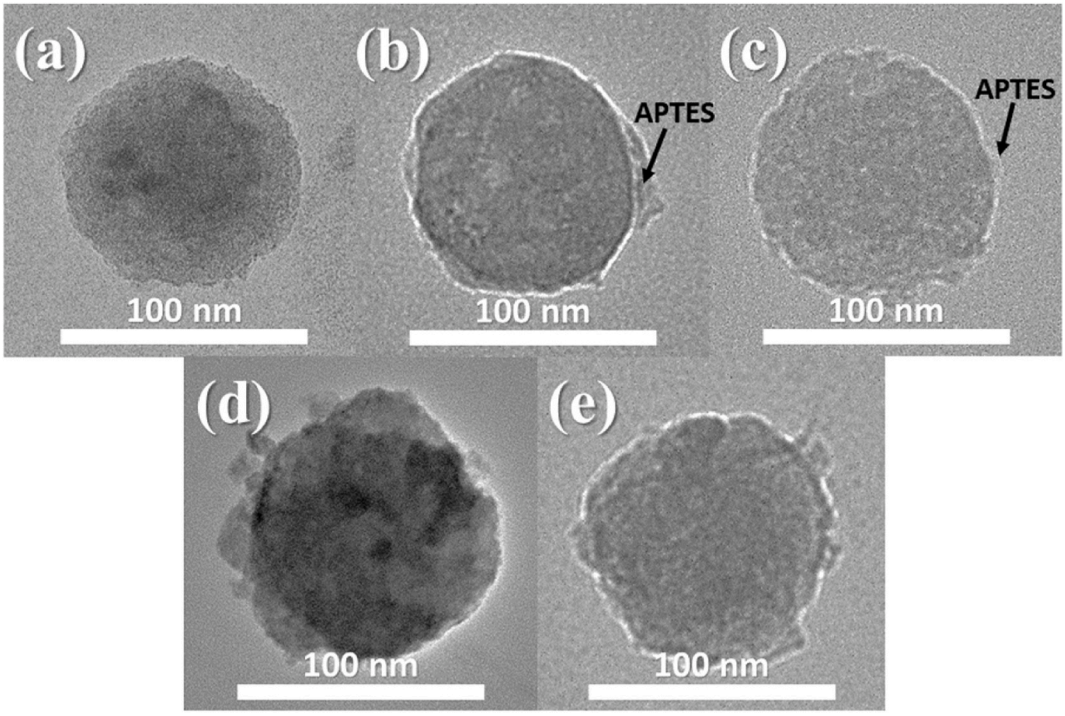


**Fig. 9.** TEM images of (a) $ST_1$, (b) $ST_1N$, (c) $ST_1N/Ni_{10}$, (d) $ST_1N/Cu_{10}$, and (e) $ST_1N/Ni_2Cu$.

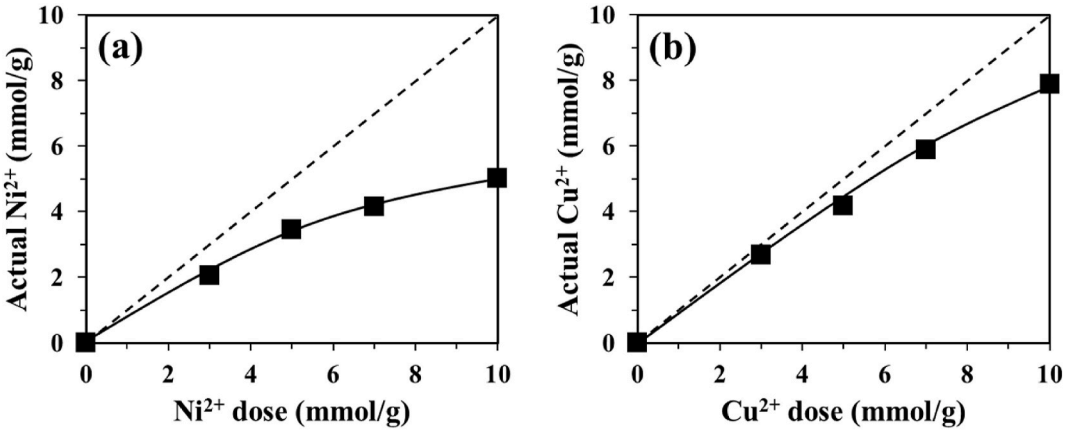


**Fig. 10.** Actual amounts of (a) $Ni^{2+}$ in $ST_1N/Ni_x$ and (b) $Cu^{2+}$ in $ST_1N/Cu_y$ determined by ICP-AES, while dose is initial amount added during catalyst preparation.

was presumably APTES (Fig. 9b). After the subsequent introduction of $Ni^{2+}$ (Fig. 9c), no clear dark spots derived from aggregated Ni species were observed, which was consistent with that $Ni^{2+}$ was highly dispersed in $ST_1N/Ni_{10}$. In contrast, the introduction of $Cu^{2+}$ brought about the formation of dark indistinct-shaped portions on the particle (Fig. 9d). Taken together with the XRD pattern of $ST_1N/Cu_{10}$, those dark portions could be $Cu(OH)_2$ particles. In the case of $ST_1N/Ni_2Cu$ (Fig. 9e), such dark portions were not so clear, though $Cu(OH)_2$ particles were present in it, which might be due to the less amount of $Cu^{2+}$ in $ST_1N/Ni_2Cu$ than that in $ST_1N/Cu_{10}$ (shown later).

Fig. 10a and b shows actual amounts of $Ni^{2+}$ and $Cu^{2+}$ present in $ST_1N/Ni_x$ and $ST_1N/Cu_y$, respectively. Table 3 summarizes doses and actual amounts of $Ni^{2+}$ and $Cu^{2+}$, and the actual $Ni^{2+}/Cu^{2+}$ ratio for $ST_1N/Ni_xCu_y$. In a series of $ST_1N/Ni_x$ (Fig. 10a), the actual amount of $Ni^{2+}$ was increased along with an increase in the $Ni^{2+}$ dose, but the actual amount was always lower than its dose, meaning that only a part of the dosing $Ni^{2+}$ was immobilized in $ST_1N/Ni_x$. This was probable because the interaction between $Ni^{2+}$ and the surface of $ST_1N$ was not so strong or only a limited number of the amino group, which was a strong binding site for $Ni^{2+}$, was present on $ST_1N$. According to the chemical elemental analysis, $ST_1N$ contained 1.59 wt% of nitrogen which corresponded to 1.06 mmol/g.

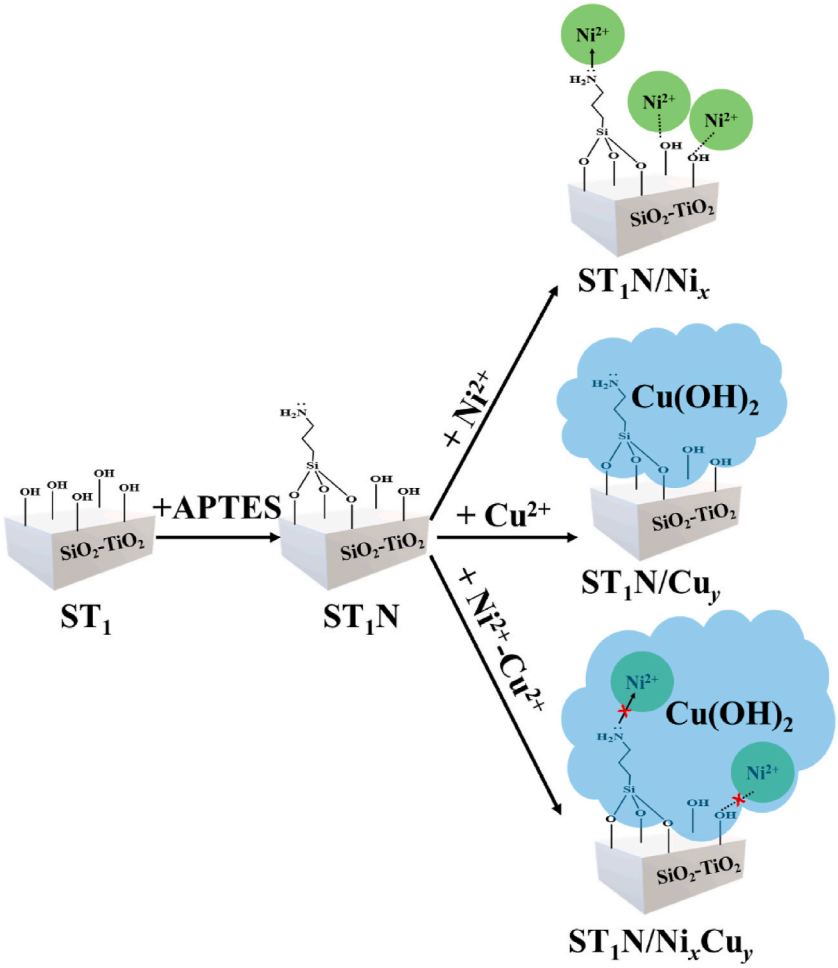


**Fig. 11.** Plausible structures of $ST_1N/Ni_x$, $ST_1N/Cu_y$, and $ST_1N/Ni_xCu_y$.

Therefore, at least the latter was plausible. In addition, since more amount of $Ni^{2+}$ was immobilized than that of the amino group in $ST_1N/Ni_x$, the former was also possible. In other words, a part of $Ni^{2+}$ was directly immobilized on the surface of the $SiO_2$–$TiO_2$ without amino group.

In a series of $ST_1N/Cu_y$ (Fig. 10b), the actual $Cu^{2+}$ amount was almost the same as the $Cu^{2+}$ dose, and this was due to the formation of $Cu(OH)_2$ unlike for $ST_1N/Ni_x$. In the case of $ST_1N/Ni_xCu_y$ (Table 3), it is noted that the actual amounts of $Ni^{2+}$ and $Cu^{2+}$ did not change when the doses of $Ni^{2+}$ and $Cu^{2+}$ were varied, resulting in the almost constant value of the actual $Ni^{2+}/Cu^{2+}$ ratio regardless of the doses of $Ni^{2+}$ and $Cu^{2+}$. Based on those characterization data and discussion so far, we propose the structures of $ST_1N/Ni_x$, $ST_1N/Cu_y$, and $ST_1N/Ni_xCu_y$ as Fig. 11. APTES was attached to $SiO_2$–$TiO_2$ through condensation between its silane group and silanol or titanol of $SiO_2$–$TiO_2$, making the amino group of APTES exposed to outer surface. In the case of $ST_1N/Ni_x$, $Ni^{2+}$ was immobilized on the surface by the formation of coordination bond with amino groups or physical interaction with hydroxyl groups. On the other hand, due to the different formation behaviour of the hydroxides, $Cu^{2+}$ in $ST_1N/Cu_y$ was precipitated as bulk $Cu(OH)_2$ on the surface, failing to bind with either amino groups or hydroxyl groups. The formation of bulk $Cu(OH)_2$ on the catalyst surface inhibited the binding of $Ni^{2+}$ and instead buried it, as shown in the $ST_1N/Ni_xCu_y$ structure.

Then, the catalytic performances of the prepared catalysts were evaluated with an ultrasound-assisted-Kumada cross-coupling reaction. First, reaction conditions including reaction time and temperature, and catalyst dose were optimized. Fig. 12 shows catalytic reaction data of $ST_1N/Ni_{10}$ for the reaction with different reaction times and temperature, and catalyst dose. As Fig. 12a shows, almost 100 % conversion was achieved at 90 min. At the time, the yield of the product (biphenyl) was 98 %, indicating that the reaction proceeded with very high selectivity. Separately, we also performed the reaction with mechanical mixing using a magnetic stirrer and the conditions other than the mixing manner were the same as those for the reaction in Fig. 12a. With the mechanical mixing, yield at 90 min was only 33 %. The higher yield obtained by the sonication-mixing was mainly caused by high energy input from high-frequency soundwave. Sonication led to intense localized heating, pressure changes, microscale turbulence, and efficient reactant mixing, and thus, it is known that some reactions proceeded more optimally [55,62,78]. In our reaction, a similar positive effect would have been achieved by the sonication-mixing.

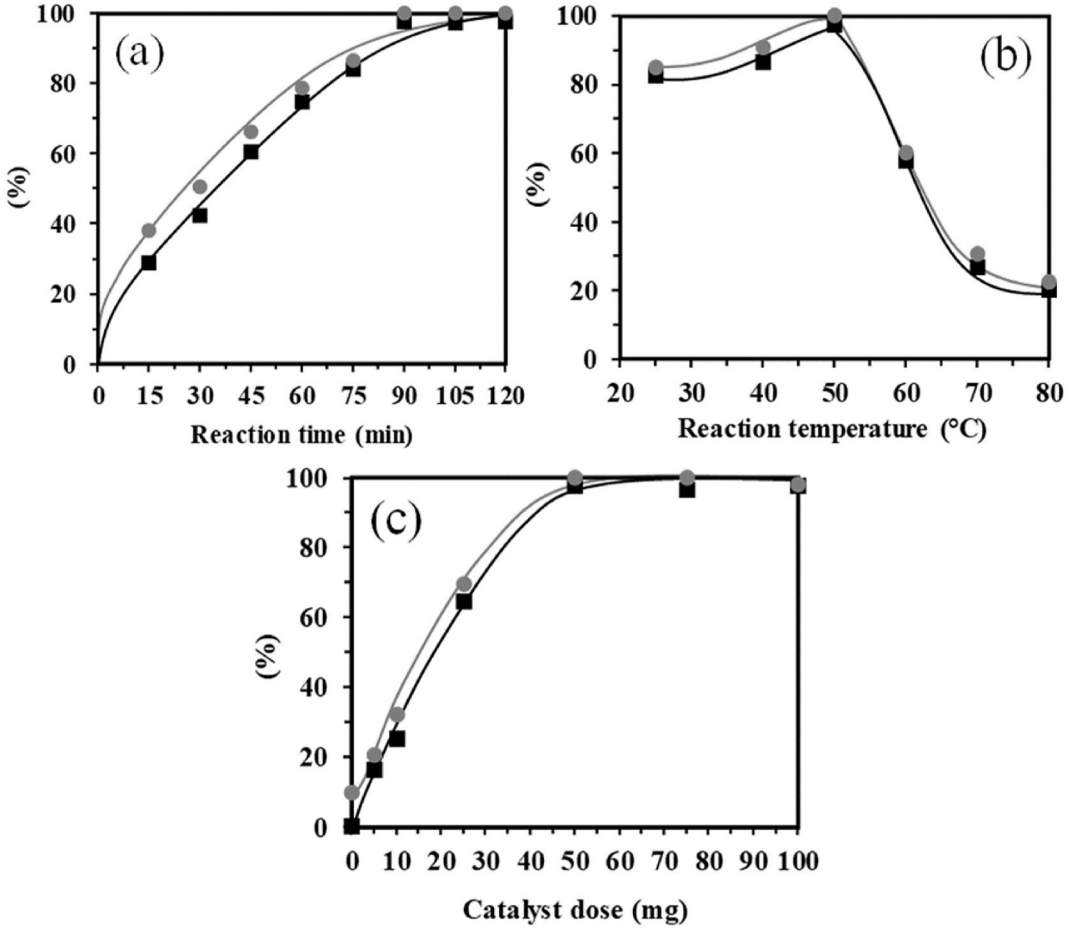


**Fig. 12.** Catalytic performance of $ST_1N/Ni_{10}$ for Kumada cross-coupling reaction. (●) conversion and (■) yield. Influences of (a) reaction time, (b) reaction temperature, and (c) catalyst dose. Reaction conditions: PhMgBr and BrPh, 1 mmol each; solvent, deoxygenated THF 2 mL; reaction temperature, 50 °C for (a) and (c); reaction time, 90 min for (b) and (c); and catalyst dose, 50 mg for (a) and (b).

**Table 4**
The catalytic activity of $ST_1N/Ni_x$ with different $Ni^{2+}$ loadings, $ST_1N/Cu_y$ with different $Cu^{2+}$ loadings, and $ST_1N/Ni_xCu_y$ with different $Ni^{2+}/Cu^{2+}$ ratios. Metal loading for each sample was determined by ICP-AES.

| Catalyst | Metal loading (mol%) | | Conversion | Yield |
|---|---|---|---|---|
| | $Ni^{2+}$ | $Cu^{2+}$ | (%) | (%) |
| $ST_1N/Ni_3$ | 0.10 | – | 45 | 39 |
| $ST_1N/Ni_5$ | 0.17 | – | 72 | 61 |
| $ST_1N/Ni_7$ | 0.21 | – | 89 | 82 |
| $ST_1N/Ni_{10}$ | 0.25 | – | 100 | 98 |
| $ST_1N/Cu_3$ | – | 0.14 | 33 | 23 |
| $ST_1N/Cu_5$ | – | 0.21 | 46 | 37 |
| $ST_1N/Cu_7$ | – | 0.30 | 57 | 45 |
| $ST_1N/Cu_{10}$ | – | 0.40 | 78 | 69 |
| $ST_1N/NiCu_2$ | 0.075 | 0.150 | 54 | 38 |
| $ST_1N/NiCu$ | 0.075 | 0.145 | 64 | 56 |
| $ST_1N/Ni_2Cu$ | 0.075 | 0.135 | 80 | 75 |

Reaction conditions: catalyst, 50 mg; reactants, PhMgBr and BrPh, 1 mmol each; solvent, deoxygenated THF, 2 mL; temperature, 50 °C; time, 90 min; and mixing method, sonication.

As Fig. 12b shows, the conversion and yield were increased with an increase in the reaction temperature up to 50 °C. However, the conversion and yield declined when the temperature was further increased. This decline at high reaction temperature was probably due to catalyst deactivation caused by the leaching of Ni species from the catalyst as reported in our previous paper [26]. Some previous literatures [63,79–81] demonstrate that employing higher temperatures in cross-coupling reactions induced side reactions,

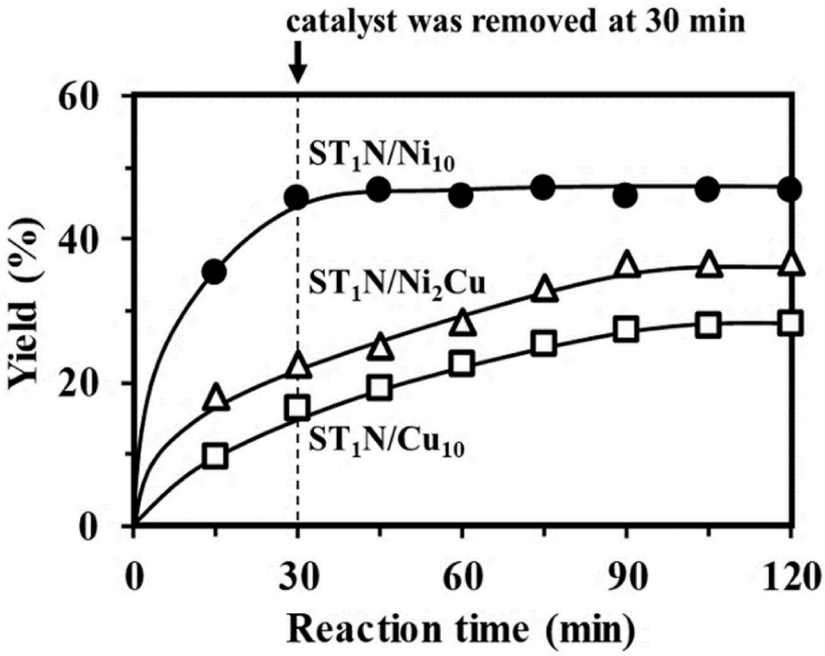


**Fig. 13.** Hot filtration test on $ST_1N/Ni_{10}$, $ST_1N/Cu_{10}$, and $ST_1N/Ni_2Cu$ during Kumada cross-coupling reaction. Reaction conditions: catalyst, 50 mg; reactants, PhMgBr and BrPh, 1 mmol each; solvent, deoxygenated THF, 2 mL; temperature, 50 °C; and mixing method, sonication.

destabilized reactants, and degraded products. Fig. 12c depicts the influence of catalyst dose on the reaction. As expected, the conversion and yield were increased with an increase in the catalyst dose, and almost 100 % conversion was achieved with 50 mg of the catalyst under the reaction conditions. Based on these results, we determined the optimal reaction conditions to be 90 min, 50 °C, and 50 mg of catalyst dose for an ultrasound-assisted-Kumada cross-coupling reaction of 1 mmol of PhMgBr and PhBr, with the isolated product as pure biphenyl as shown by $^1$H NMR spectra in Fig. S5; $^1$H NMR (500 MHz) δ 7.32–7.35 (m, 2H), 7.41–7.44 (m, 4H), and 7.58–7.59 (m, 4H).

Next, we optimized the solvent for the reaction using $ST_1N/Ni_{10}$ as a model catalyst. Table S1 summarizes the results of the reaction performed in different solvents. The reaction proceeded in all the solvents examined in this study with moderate to high yield of the product. Among them, tetrahydrofuran and acetonitrile were the best and second-best solvents, respectively, in terms of yield. Therefore, subsequent reaction experiments were performed using THF as a solvent. THF was also used for the reactions shown in Fig. 12.

Having optimized the reaction conditions, then we investigated the influence of metals ($Ni^{2+}$ and $Cu^{2+}$) and metal loadings on the catalytic performance. The results are summarized in Table 4. $ST_1N/Ni_x$ was superior in the catalytic performance to $ST_1N/Cu_y$, while catalytic performances were improved as the metal loadings were increased regardless of the metal cation. Furthermore, $ST_1N/Ni_{10}$ showed better performance than $ST_1N/Ni_xCu_y$. As had been already demonstrated, $Ni^{2+}$ was highly dispersed on $ST_1N/Ni_{10}$, while $Cu^{2+}$ agglomerated to form $Cu(OH)_2$ particles on $ST_1N/Cu_{10}$ and $ST_1N/Ni_xCu_y$. Such differences in the existing state of the metal species caused that in the catalytic performance.

In addition to the high catalytic activity, $ST_1N/Ni_{10}$ had an essential property as a heterogeneous catalyst, which is the high stability of active metal species under the reaction conditions. To investigate the stability of the catalysts, a hot filtration test and catalyst reuse experiment were conducted. Fig. 13 shows the results of hot filtration experiments with $ST_1N/Ni_{10}$, $ST_1N/Cu_{10}$, and $ST_1N/Ni_2Cu$. At 30 min, all catalyst powder was removed from each reaction solution and the reaction was further continued at 50 °C. It is noted that the reaction was completely stopped after the removal of $ST_1N/Ni_{10}$, demonstrating that only the heterogenous catalytic reaction occurred on this catalyst. In contrast, in the case of $ST_1N/Cu_{10}$ and $ST_1N/Ni_2Cu$, the biphenyl yield continued increasing even after the removal of the catalyst powder. This indicated that $ST_1N/Cu_{10}$ and $ST_1N/Ni_2Cu$ were less stable under the reaction conditions, generating catalytically active species in the reaction solution, which is a fatal problem in heterogeneous catalysts. The interaction between $Ni^{2+}$ and the amino group through a coordination bond and that between $Ni^{2+}$ and the surface of the $SiO_2$–$TiO_2$ were strong enough to prevent the leaching of the catalytically active Ni species, bringing about the high stability of this catalyst.

We explored the substrate scope of the ultrasound-assisted-Kumada cross-coupling reaction in the presence of $ST_1N/Ni_{10}$ (Table 5). We initially evaluated the nature of phenyl halide to the performance of $ST_1N/Ni_{10}$ in the Kumada cross-coupling. We were pleased to obtain the biphenyl product in excellent yield when the reaction was performed using phenyl magnesium bromide and phenyl bromide as the substrates (entry 1). It should be noted that the reaction proceeded even with fluorobenzene (entry 2) and chlorobenzene (entry 3), although the yields were somewhat lower than those with bromobenzene (entry 1). The possible reactions with fluorobenzene and chlorobenzene were likely caused by the sonication effect. As explained before, sonication can produce strong localized heating and

**Table 5**
Substrate scope of ultrasound-assisted-Kumada cross-coupling reaction catalyzed by $ST_1N/Ni_{10}$.

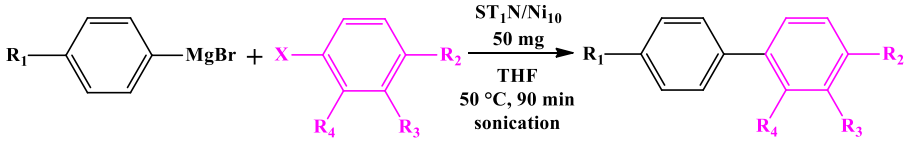


| Entry | $R_1$ | $R_2$ | $R_3$ | $R_4$ | X | Product | Yield[b] |
|---|---|---|---|---|---|---|---|
| 1 | H | H | H | H | Br | 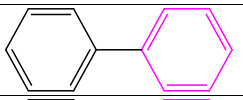 | 98 |
| 2 | H | H | H | H | F | 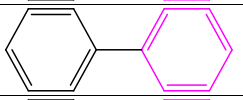 | 65 |
| 3 | H | H | H | H | Cl | 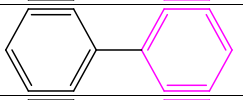 | 80 |
| 4 | H | H | H | H | I | 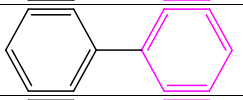 | 72 |
| 5 | H | H | H | H | $CH_3SO_2$ | 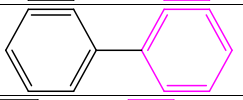 | 90 |
| 6 | H | $CH_3$ | H | H | Br | 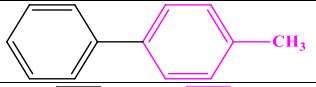 | 84 |
| 7 | H | H | $CH_3$ | H | Br |  | 72 |
| 8 | H | H | H | $CH_3$ | Br | 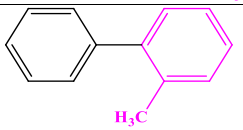 | 66 |
| 9 | $CH_3$ | $CH_3$ | H | H | Br | 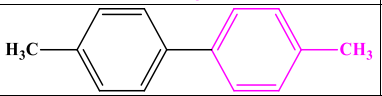 | 80 |
| 10 | $CH_3$ | H | $CH_3$ | H | Br | 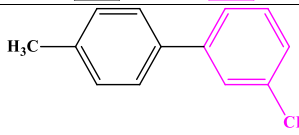 | 64 |
| 11 | H | $NO_2$ | H | H | Br | 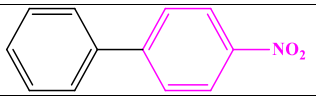 | 98 |
| 12 | H | H | $NO_2$ | H | Br | 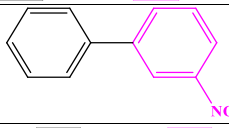 | 88 |
| 13 | $CH_3$ | $NO_2$ | H | H | Br | 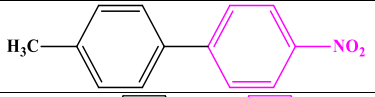 | 88 |
| 14 | $CH_3$ | H | $NO_2$ | H | Br | 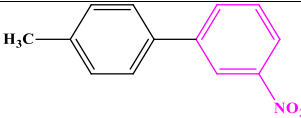 | 81 |

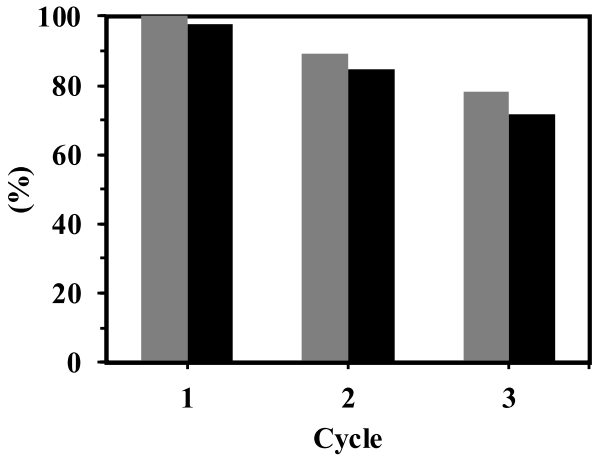


**Fig. 14.** Reusability test for $ST_1N/Ni_{10}$. (■) conversion and (■) yield. Reaction conditions: catalyst, 50 mg; reactants, PhMgBr and BrPh, 1 mmol each; solvent, deoxygenated THF, 2 mL; temperature, 50 °C; time, 90 min; and mixing method, sonication. The catalyst recycling process was carried out by collecting the used catalyst by filtration, continued by washing the catalyst with THF, ethanol, and water three times for each, and then drying it at 60 °C for 12 h.

**Table 6**
Catalytic performances of $ST_1N/Ni_{10}$ and the related materials.

| Catalyst | Conversion (%) | Yield (%) |
|---|---|---|
| $SiO_2$ | 11 | 0 |
| $TiO_2$ | 3 | 0 |
| $ST_1$ | 32 | 0 |
| $ST_1N$ | 11 | 0 |
| $SiO_2$/Ni | 33 | 30 |
| $TiO_2$/Ni | 34 | 32 |
| $ST_1$/Ni | 54 | 47 |
| $SiO_2$-APTES/Ni | 81 | 79 |
| $TiO_2$-APTES/Ni | 87 | 83 |
| $ST_1N/Ni_{10}$ | 100 | 98 |
| without catalyst (blank) | 10 | 0 |

Reaction conditions: catalyst, 50 mg; reactants, PhMgBr and BrPh, 1 mmol each; solvent, deoxygenated, 2 mL; temperature, 50 °C; time, 90 min; and mixing method, sonication.

pressure changes which might cause the bond in fluorobenzene and chlorobenzene to break thus the reaction proceeded, whereas in usual, it is quite difficult. In addition, phenyl iodide and phenyl methanesulfonate were also compatible with the reaction conditions, generating the desired product in good yield (entries 4–5).

Phenyl bromides bearing electron-donating ($CH_3$) or withdrawing ($NO_2$) groups were suitable for the ultrasound-assisted-Kumada cross-coupling reaction, where the latter produced the biphenyl product in higher yields (Table 5, entry 6 vs 9). We found that *para*-substituted phenyl bromides generated the corresponding products in higher yields, compared with *meta*- and *ortho-substituted* phenyl bromides (entry 6 vs 7 vs 8 and entry 9 vs 10). The results indicated that the Kumada cross-coupling was affected by the steric hindrance of phenyl halides.

To enlarge the scope of our methodology, we utilized the Grignard reagent of tolylmagnesium bromide (Table 5, entry 11–14). Similarly, the inductive and steric effects of phenyl bromides influenced the ultrasound-assisted-Kumada cross-coupling, where phenyl bromide substituted with the electron-withdrawing group ($NO_2$) at the *para* position gave the product in higher yield (entry 13).

The high stability of $ST_1N/Ni_{10}$ was also demonstrated for the reusability test. As shown in Fig. 14, $ST_1N/Ni_{10}$ exhibited decent catalytic activity even on the third use (second reuse), although the performance slightly declined with reuse. The slight decline of the catalyst performance with reuse might be brought about by the accumulation of the product and/or the reactants, which was demonstrated by the TG profile of the spent catalyst (Fig. S4), while the surface area of the catalyst was not changed with the reuse (Fig. S4 and Table S2).

Next, we discussed the need for each component in $ST_1N/Ni_{10}$ for the reaction. We prepared materials without at least one component that made up $ST_1N/Ni_{10}$ in a similar manner to that for $ST_1N/Ni_{10}$ and evaluated their catalytic performances. Table 6 lists the catalytic performance of those materials for ultrasound-assisted-Kumada cross-coupling reaction. Support materials themselves without $Ni^{2+}$, namely $SiO_2$, $TiO_2$, $ST_1$, and $ST_1N$, did not produce the product at all. On the other hand, the materials with $Ni^{2+}$ showed catalytic activity and the product was formed, but the yields were lower than that for $ST_1N/Ni_{10}$, specifically, the yields for $ST_1$/Ni, $SiO_2$-APTES/Ni, and $TiO_2$-APTES/Ni were 47, 49, and 83 %, respectively, while that for $ST_1N/Ni_{10}$ was 98 %. These results

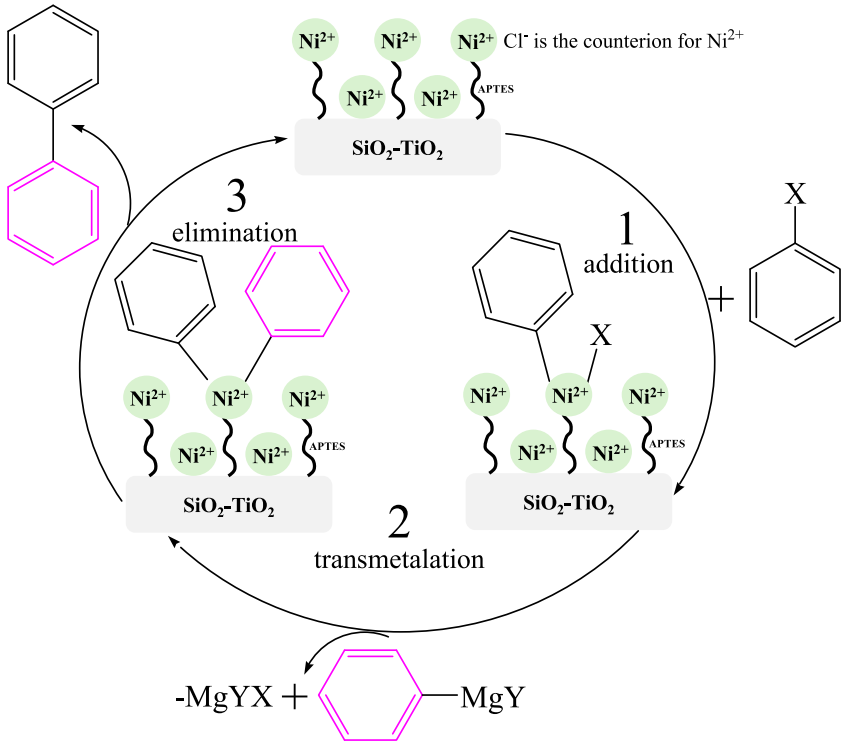


**Fig. 15.** Proposed mechanism of Kumada cross-coupling reaction catalyzed by $ST_1N/Ni_{10}$.

**Table 7**
Comparison of $ST_1N/Ni_{10}$ catalytic performance with previously reported catalysts for biphenyl synthesis reaction.

| Catalyst | Conditions | Yield | References |
|---|---|---|---|
| Ni(II)RGO | 60 °C; 5 h; 0.1 mol% Ni(II) catalyst; 1.0 mmol 4-iodoanisole; 1.8 mmol PhMgCl; THF[a]; reflux | 62 | [82] |
| Ni(0)RGO | 60 °C; 5 h; 0.1 mol% Ni(0) catalyst; 1.0 mmol 4-iodoanisole; 1.8 mmol PhMgCl; THF[a]; reflux | 92 | [82] |
| Merrifield resin-Ni(II) complex | r.t.; 24 h; 0.5 mol% Ni(II) catalyst; 0.5 mmol $CH_3OPhBr$; 0.5 mmol PhMgBr; THF[a]; reflux | 73 | [83] |
| Pd@MCF(Sn) | 55 °C; 60 min; 0.4 mol% Pd catalyst; 0.2 mmol PhI; 0.24 mmol $PhB(OH)_2$; $H_2O$:EtOH (1:1); sonication | 100 | [84] |
| Cell-Sc-Pd(II) | 70 °C; 30 min; 0.0016 mol% Pd catalyst; 1.0 mmol PhI; 0.11 mmol $PhB(OH)_2$; $H_2O$:EtOH (1:1); reflux | 94 | [85] |
| Pd@HKUST-1 | 70 °C; 7 h; 0.001 mol% Pd catalyst; 1.0 mmol PhI; 1.0 mmol $PhB(OH)_2$; toluene; reflux | 82 | [86] |
| GO-$N_2S_2$/Pd | 75 °C; 3 h; 0.5 mol% Pd catalyst; 1 mmol PhI; 1.2 mmol $PhB(OH)_2$; EtOH; reflux | 94 | [87] |
| $Fe_3O_4$@CS-Co | 100 °C; 3 h; 2 mol% Co catalyst; 1 mmol PhI; 1.1 mmol $PhSi(OEt)_3$; DMF[a]; reflux | 91 | [88] |
| $Fe_3O_4$@$SiO_2$-T-Se/Pd(II) | 60 °C; 30 min; 0.04 mol% Pd(II) catalyst; 1 mmol PhI; 1.1 mmol $PhB(OH)_2$; $H_2O$:EtOH (1:2); reflux | 95 | [89] |
| $ST_1N/Ni_{10}$ | 50 °C; 90 min; 0.25 mol% $Ni^{2+}$ catalyst; 1 mmol PhBr; 1 mmol PhMgBr; THF[a]; sonication | 98 | This work |

[a] THF, tetrahydrofuran; and DMF, dimethylformamide.

demonstrated that each component in $ST_1N/Ni_{10}$, including $SiO_2$ and $TiO_2$ (components of the support material), APTES (strong binding site for $Ni^{2+}$), and $Ni^{2+}$ (active species), had a significant role in enhancing the catalytic performance for the reaction.

We proposed the reaction mechanism for Kumada cross-coupling reaction catalyzed by $ST_1N/Ni_{10}$ based on the previous studies [12,26], and the role of each component in the catalyst in supporting the catalytic performance. As can be seen in Fig. 15, $Ni^{2+}$ was the active species where Kumada cross-coupling reaction took place. These active species were first immobilized on APTES-functionalized $SiO_2$–$TiO_2$. APTES had a role as a binding site for $Ni^{2+}$ so that $Ni^{2+}$ was dispersed on the surface not only by weak physical interaction (with hydroxyl groups of silanol and titanol on $SiO_2$–$TiO_2$ support) but also by stronger coordination bond (with amino groups of APTES). The Kumada cross-coupling reaction occurring on $Ni^{2+}$ active sites started from the addition step (number 1) where halobenzene was bound to $Ni^{2+}$ and a halo(phenyl)nickel complex was formed. Subsequently, the attached halide on $Ni^{2+}$ was replaced by phenyl from the Grignard reagent through the transmetalation step (number 2) which gave a diphenylnickel complex. Lastly, these two phenyls were released to form biphenyl through the elimination step (number 3). The cycle continued until all reactants were totally consumed.

Finally, we have compiled data from prior studies on biphenyl synthesis reactions catalyzed by nickel-, cobalt-, and palladium-modified catalysts in Table 7. Palladium consistently exhibited superior catalytic performance compared to other metal catalysts, producing high biphenyl yields due to its inherently high catalytic activity. Despite nickel catalysts demonstrating lower efficiency than palladium catalysts, they remain more beneficial due to their economic viability. Additionally, our catalyst, $ST_1N/Ni_{10}$,

demonstrated comparable catalytic performance under mild conditions, achieving a high biphenyl yield of 98 %.

## 4. Conclusions

In the present study, first, we prepared $SiO_2$–$TiO_2$ in the presence of cetyltrimethylammonium bromide (CTAB) as a particle growth inhibitor. In the presence of the optimum amount of CTAB, which was an equimolar amount of $SiO_2$–$TiO_2$, fine particles of $SiO_2$–$TiO_2$ with an average size of 146 nm and surface area of 502 $m^2$ $g^{-1}$ were obtained. The average particle size and surface area of the $SiO_2$–$TiO_2$ fine particles were about half and twice, respectively, of those previously reported $SiO_2$–$TiO_2$ prepared in the presence of polyethylene glycol.

Then, the $SiO_2$–$TiO_2$ fine particles were modified with (3-aminopropyl)triethoxysilane ($ST_1N$), and $Ni^{2+}$, $Cu^{2+}$, or both of them were immobilized on $ST_1N$. $Ni^{2+}$ was highly dispersed on $ST_1N$ without the formation of crystalline nickel compounds, and the obtained catalyst ($ST_1N/Ni_{10}$) showed high catalytic activity for ultrasound-assisted-Kumada cross-coupling reaction to form biphenyls and was reusable at least three times. In contrast, $Cu^{2+}$ was aggregated on $ST_1N$ as crystalline $Cu(OH)_2$, and the resulting $Cu^{2+}$ catalysts and those having both $Cu^{2+}$ and $Ni^{2+}$ were less active for the reaction and less stable under the reaction conditions that the catalytically active species were dissolved into the reaction solution.

The sonication-mixing was very effective in promoting the Kumada cross-coupling reaction, and the time required to complete the reaction was reduced to about one-fourth of that required for the conventional mechanical mixing using a magnetic stirrer. $ST_1N/Ni_{10}$ promoted ultrasound-assisted-Kumada cross-coupling reactions of a wide variety of substrates.

## Data availability statement

The data associated with this study has not been deposited into a publicly available repository. The data included in the article/supplementary material/referenced in the article.

## CRediT authorship contribution statement

**Dewi Agustiningsih:** Writing – original draft, Methodology, Investigation, Formal analysis, Conceptualization. **Eko Sri Kunarti:** Writing – review & editing, Supervision, Formal analysis, Conceptualization. **Nuryono Nuryono:** Writing – review & editing, Supervision, Conceptualization. **Sri Juari Santosa:** Writing – review & editing, Supervision, Conceptualization. **Muhammad Idham Darussalam Mardjan:** Writing – review & editing, Conceptualization. **Yuichi Kamiya:** Writing – review & editing, Supervision, Conceptualization. **Ryoichi Otomo:** Writing – review & editing, Methodology, Formal analysis.

## Declaration of competing interest

The authors declare that they have no known competing financial interests or personal relationships that could have appeared to influence the work reported in this paper.

## Acknowledgments

The work was supported by Ministry of Research, Technology, and Higher Education Indonesia (DRTPM Kemdikbudristek) who provided PMDSU scholarship, research funding (2193/UN1/DITLIT/Dit-Lit/PT.March 01, 2023; 018/E5/PG.02.00.PL/2023) and Enhancing International Publication (EIP) - Peningkatan Kualitas Publikasi Internasional (PKPI) program 2023 (106.7/E4.4/KU/2023).

We thank the Open Facility, Global Facility Center, Creative Research Institute, Hokkaido University for allowing us to analyze with ICP-AES and providing insight and expertise that greatly assisted the research. A part of this work was conducted at the Laboratory of XPS analysis, Joint-use facilities, Hokkaido University.

## Appendix A. Supplementary data

Supplementary data to this article can be found online at https://doi.org/10.1016/j.heliyon.2024.e34614.

## References

[1] N.A.I. Md Ishak, S.K. Kamarudin, S.N. Timmiati, S. Mohd Sauid, N. A Karim, S. Basri, Green synthesis of platinum nanoparticles as a robust electrocatalyst for methanol oxidation reaction: metabolite profiling and antioxidant evaluation, J. Clean. Prod. 382 (2023) 1–18, https://doi.org/10.1016/j.jclepro.2022.135111.

[2] M. Wu, M. Miao, W. Li, X. Zhang, L. Zhang, T. Zhen, Y. Fu, J. Jin, L. Yuan, Metal-organic framework-derived one-dimensional Pd@$CeO_2$ catalysts with enhanced activity for methane oxidation, Fuel 331 (2023) 1–10, https://doi.org/10.1016/j.fuel.2022.125575.

[3] X. Zhang, Y. Yu, T. Lin, B. Xu, H. Xu, S. Zhu, Small-size MOF derived highly active low-platinum catalysts for oxygen reduction reactions, J. Solid State Chem. 322 (2023) 1–10, https://doi.org/10.1016/j.jssc.2023.123899.

[4] A.M. Elsharif, M.A. Almarzooq, T.A. Saleh, Synthesis and characterization of gold nanohybrid and its efficiency for benzaldehyde reduction, J. Mol. Struct. 1289 (2023) 1–8, https://doi.org/10.1016/j.molstruc.2023.135790.

[5] K.V. Deriabin, E.A. Golovenko, N.S. Antonov, S.V. Baykov, V.P. Boyarskiy, R.M. Islamova, Platinum macrocatalyst for heterogeneous Si-O dehydrocoupling, Dalton Trans. 52 (2023) 5854–5858, https://doi.org/10.1039/d3dt00651d.

[6] H. Miura, M. Doi, Y. Yasui, Y. Masaki, H. Nishio, T. Shishido, Diverse alkyl-silyl cross-coupling via homolysis of unactivated C($sp^3$)-O bonds with the cooperation of gold nanoparticles and amphoteric zirconium oxides, J. Am. Chem. Soc. 145 (2023) 4613–4625, https://doi.org/10.1021/jacs.2c12311.

[7] T.N. Ansari, F. Gallou, S. Handa, Palladium-catalyzed micellar cross-couplings: an outlook, Coord. Chem. Rev. 488 (2023) 1–17, https://doi.org/10.1016/j.ccr.2023.215158.

[8] M. Kumar, K. Kaliya, S.K. Maurya, Recent progress in the homogeneous gold-catalysed cycloisomerisation reactions, Org. Biomol. Chem. 21 (2023) 3276–3295, https://doi.org/10.1039/d2ob02015g.

[9] B.H. Lipshutz, On the sustainability of palladium in organic synthesis: a perspective, Johnson Matthey Technol. Rev. 67 (2023) 278–284, https://doi.org/10.1595/205651323X16698159435916.

[10] M. Yadav, R.K. Sharma, Heterogenized nickel catalysts for various organic transformations, Curr. Opin. Green Sustainable Chem. 15 (2019) 47–59, https://doi.org/10.1016/j.cogsc.2018.08.010.

[11] V.P. Ananikov, Nickel: the "spirited horse" of transition metal catalysis, ACS Catal. 5 (2015) 1964–1971, https://doi.org/10.1021/acscatal.5b00072.

[12] K. Tamao, K. Sumitani, M. Kumada, Selective carbon-carbon bond formation by cross-coupling of grignard reagents with organic halides, Catalysis by Nickel-Phosphine Complexes, J. Am. Chem. Soc. 94 (1972) 4374–4376, https://doi.org/10.1021/ja00767a075.

[13] Á. Kiss, Z. Hell, M. Bálint, Nickel/magnesium-lanthanum mixed oxide catalyst in the Kumada-coupling, Org. Biomol. Chem. 8 (2010) 331–335, https://doi.org/10.1039/b919246h.

[14] S. Thapa, B. Shrestha, S.K. Gurung, R. Giri, Copper-catalysed cross-coupling: an untapped potential, Org. Biomol. Chem. 13 (2015) 4816–4827, https://doi.org/10.1039/c5ob00200a.

[15] H. Pandiri, R.G. Gonnade, B. Punji, Synthesis of quinolinyl-based pincer copper(II) complexes: an efficient catalyst system for Kumada coupling of alkyl chlorides and bromides with alkyl Grignard reagents, Dalton Trans. 47 (2018) 16747–16754, https://doi.org/10.1039/C8DT03210F.

[16] Y. Riadi, M.H. Geesi, O. Ouerghi, R. Azzallou, O. Dehbi, S. Lazar, Sol-gel $TiO_2$ nanostructures single doped with copper and nickel as nanocatalysts for enhanced performance for the Liebeskind–Srogl reaction, Mater. Chem. Phys. 267 (2021) 1–7, https://doi.org/10.1016/j.matchemphys.2021.124607.

[17] T.T. Wen, L.Z. Wang, $CoFe_2O_4$@$SiO_2$@APTES@HO-PBA@Cu$(OAc)_2$: a highly efficient and recyclable nanocatalyst for one-pot synthesis of multifunctional 1,5-benzodiazepines via three-component domino reaction, Mater. Today Chem. 26 (2022) 1–14, https://doi.org/10.1016/j.mtchem.2022.101071.

[18] T. Sukkasem, A. Nuchitprasittichai, S. Junpirom, N. Pulsawat, P. Khumronrith, S. Photongngam, P. Janphuang, Role of $SiO_2$ in $TiO_2$/$SiO_2$ photocatalyst for hydrogen peroxide gas generation from air humidity via photocatalysis, J. Inclusion Phenom. Macrocycl. Chem. 2 (2023), https://doi.org/10.1007/s10847-023-01211-3.

[19] X. Yu, C.T. Williams, Recent advances in the applications of mesoporous silica in heterogeneous catalysis, Catal. Sci. Technol. 12 (2022) 5765–5794, https://doi.org/10.1039/d2cy00001f.

[20] P.S. Shinde, P.S. Suryawanshi, K.K. Patil, V.M. Belekar, S.A. Sankpal, S.D. Delekar, S.A. Jadhav, A brief overview of recent progress in porous silica as catalyst supports, J. Compos. Sci. 5 (2021) 1–17, https://doi.org/10.3390/jcs5030075.

[21] M.Z. Sarker, M.M. Rahman, H. Minami, T. Suzuki, H. Ahmad, Amine functional silica–supported bimetallic Cu-Ni nanocatalyst and investigation of some typical reductions of aromatic nitro-substituents, Colloid Polym. Sci. 300 (2022) 279–296, https://doi.org/10.1007/s00396-021-04910-w.

[22] M.E. Ali, M.M. Rahman, S.M. Sarkar, S.B.A. Hamid, Heterogeneous metal catalysts for oxidation reactions, J. Nanomater. 2014 (2014), https://doi.org/10.1155/2014/192038.

[23] S. Bagheri, N. Muhd Julkapli, S. Bee Abd Hamid, Titanium dioxide as a catalyst support in heterogeneous catalysis, Sci. World J. 2014 (2014) 1–24, https://doi.org/10.1155/2014/727496.

[24] D. Agustiningsih, N. Nuryono, S.J. Santosa, E.S. Kunarti, Propylamine silica-titania hybrid material modified with Ni(II) as the catalyst for benzyl alcohol to benzaldehyde conversion, Indones. J. Chem. 23 (2023) 1361–1374, https://doi.org/10.22146/ijc.84282.

[25] S. Viéitez-Calo, D.J. Morgan, S. Golunski, S.H. Taylor, M.V. Twigg, Structure sensitivity and hydration effects in Pt/$TiO_2$ and Pt/$TiO_2$–$SiO_2$ catalysts for NO and propane oxidation, Top. Catal. 64 (2021) 955–964, https://doi.org/10.1007/s11244-021-01415-2.

[26] D. Agustiningsih, R. Otomo, Y. Kamiya, N. Nuryono, S.J. Santosa, E.S. Kunarti, Fixing $Ni^{2+}$ onto mesoporous $SiO_2$-$TiO_2$ through amino silane and application as a catalyst for Kumada cross coupling reaction for 1,1′-biphenyl synthesis, Appl. Catal. Gen. 672 (2024) 1–11, https://doi.org/10.1016/j.apcata.2024.119606.

[27] S. Hegde, A. Nizam, A. Vijayan, R.B. Dateer, S.B.N. Krishna, Palladium immobilized on guanidine functionalized magnetic nanoparticles: a highly effective and recoverable catalyst for ultrasound aided Suzuki-Miyaura cross-coupling reactions, New J. Chem. 47 (2023) 18856–18864, https://doi.org/10.1039/d3nj03444e.

[28] P. Han, S. Zhu, W. Zhang, B. Yang, D. Huang, R. Ren, T. Li, M. Liu, Y. Wu, Pd/$Co_3O_4$-Pd/PdO formed in situ on the surface of the self-assembly ferrocenylimine Pd(II)/Co(II) monolayer for catalyzing the Suzuki cross-coupling reaction—formation, synergistic effect, and catalytic mechanism, New J. Chem. 47 (2023) 8426–8438, https://doi.org/10.1039/d3nj00457k.

[29] P.B. Rathod, K.S. Ajish Kumar, M. Pratap Singh, A.A. Athawale, A.K. Pandey, Pd(II)-Functionalized polymeric shell encapsulated on magnetite nanocatalysts for C–C coupling reactions, ChemistrySelect 7 (2022) 1–7, https://doi.org/10.1002/slct.202202029.

[30] L. Paul, S. Chatterjee, S. Mukherjee, T. Sen, A. Bhaumik, Cu(II)-grafted 2D-hexagonal mesoporous material as an efficient catalyst for Sonogashira C-C cross-coupling reaction, Mater. Today Proc. 45 (2020) 3733–3740, https://doi.org/10.1016/j.matpr.2020.12.1156.

[31] Y. Wang, D. Hu, R. Guo, H. Deng, M. Amer, Z. Zhao, H. Xu, K. Yan, Facile synthesis of Ni/$Fe_3O_4$ derived from layered double hydroxides with high performance in the selective hydrogenation of benzaldehyde and furfural, Mol. Catal. 528 (2022) 1–7, https://doi.org/10.1016/j.mcat.2022.112505.

[32] S. Hegde, A. Nizam, A. Vijayan, Furaldehyde-based magnetic supported palladium nanoparticles as an efficient heterogeneous catalyst for Mizoroki-Heck cross-coupling reaction, New J. Chem. (2023) 1121–1129, https://doi.org/10.1039/d3nj04868c.

[33] N. Amirmahani, N.O. Mahmoodi, M. Malakootian, A. Pardakhty, N. Seyedi, Pd nanoparticles supported on $Fe_3O_4$@$SiO_2$-Schiff base as an efficient magnetically recoverable nanocatalyst for Suzuki–Miyaura coupling reaction, Res. Chem. Intermed. 46 (2020) 4595–4609, https://doi.org/10.1007/s11164-020-04223-7.

[34] A. Landarani-Isfahani, I. Mohammadpoor-Baltork, V. Mirkhani, M. Moghadam, S. Tangestaninejad, H. Amiri Rudbari, Palladium nanoparticles immobilized on a nano-silica triazine dendritic polymer: a recyclable and sustainable nanoreactor for C-S cross-coupling, RSC Adv. 10 (2020) 21198–21205, https://doi.org/10.1039/d0ra00719f.

[35] M. Khodamorady, K. Bahrami, Design, synthesis, characterization and application of BNPs@$SiO_2$$(CH_2)_3$NH-CC-AMP-Pd (0) as a new reusable nano-catalyst for suzuki and Heck cross-coupling reactions, Catal. Lett. 150 (2020) 1571–1590, https://doi.org/10.1007/s10562-019-03054-5.

[36] B. Zuo, H. Shao, Y. Zheng, Y. Ma, W. Li, M. Huang, Q. Deng, The core-shell magnetic mesoporous microspheres immobilized NHC-palladacycles: an efficient and recyclable catalyst for suzuki-miyaura cross-coupling of pharmaceutical synthesis, Asian J. Org. Chem. 11 (2022) 1–5, https://doi.org/10.1002/ajoc.202200018.

[37] T. Baran, M. Nasrollahzadeh, Facile fabrication of magnetically separable palladium nanoparticles supported on modified kaolin as a highly active heterogeneous catalyst for Suzuki coupling reactions, J. Phys. Chem. Solid. 146 (2020) 1–8, https://doi.org/10.1016/j.jpcs.2020.109566.

[38] S.A. Jasim, M.J. Ansari, H.S. Majdi, M.J.C. Opulencia, K.F. Uktamov, Nanomagnetic Salamo-based-Pd(0) Complex: an efficient heterogeneous catalyst for Suzuki–Miyaura and Heck cross-coupling reactions in aqueous medium, J. Mol. Struct. 1261 (2022) 1–14, https://doi.org/10.1016/j.molstruc.2022.132930.

[39] H. Veisi, B. Karmakar, P. Mohammadi, T. Tamoradi, S. hemmati, Z. Joshani, Metal catalyst supported on modified Carbon Nano Tubes (CNTs) for cross-coupling reactions, Inorg. Chem. Commun. 156 (2023) 1–40, https://doi.org/10.1016/j.inoche.2023.110979.

[40] I. Dindarloo Inaloo, S. Majnooni, H. Eslahi, M. Esmaeilpour, Nickel(II) nanoparticles immobilized on EDTA-modified $Fe_3O_4$@$SiO_2$ nanospheres as efficient and recyclable catalysts for ligand-free suzuki-miyaura coupling of aryl carbamates and sulfamates, ACS Omega 5 (2020) 7406–7417, https://doi.org/10.1021/acsomega.9b04450.

[41] K. Juhász, Á. Magyar, Z. Hell, Transition-metal-catalyzed cross-coupling reactions of grignard reagents, Synth. Met. 53 (2021) 983–1002, https://doi.org/10.1055/s-0040-1705986.

[42] Z.X. Wang, Z.Y. Chai, Palladium(II) and nickel(II) complexes bearing N,N,O-chelate ligands: syntheses, characterization and catalysis in Heck and Kumada coupling reactions, Eur. J. Inorg. Chem. (2007) 4492–4499, https://doi.org/10.1002/ejic.200700347.

[43] A.C. Frisch, F. Rataboul, A. Zapf, M. Beller, First Kumada reaction of alkyl chlorides using N-heterocyclic carbene/palladium catalyst systems, J. Organomet. Chem. 687 (2003) 403–409, https://doi.org/10.1016/S0022-328X(03)00723-X.

[44] F.G. Buono, Y. Zhang, Z. Tan, A. Brusoe, B. Yang, J.C. Lorenz, R. Giovannini, J.J. Song, N.K. Yee, C.H. Senanayake, Efficient Iron-Catalyzed Kumada Cross-Coupling Reactions Utilizing Flow Technology under Low Catalyst Loadings, vol. 1, 2016, pp. 2599–2602, https://doi.org/10.1002/ejoc.201600275.

[45] E.F. Chard, L.N. Dawe, C.M. Kozak, Coupling of benzyl halides with aryl Grignard reagents catalyzed by iron(III) amine-bis(phenolate) complexes, J. Organomet. Chem. 737 (2013) 32–39, https://doi.org/10.1016/j.jorganchem.2013.03.034.

[46] Á. Kiss, J. Németh, A. Fodor, Z. Hell, Supported metal catalysts in organic syntheses, Period. Polytech. - Chem. Eng. 59 (2015) 72–81, https://doi.org/10.3311/PPch.7343.

[47] J.A. Przyojski, H.D. Arman, Z.J. Tonzetich, NHC complexes of cobalt(II) relevant to catalytic C-C coupling reactions, Organometallics 32 (2013) 723–732, https://doi.org/10.1021/om3010756.

[48] K. Matsubara, T. Sueyasu, M. Esaki, A. Kumamoto, S. Nagao, H. Yamamoto, Y. Koga, S. Kawata, T. Matsumoto, Cobalt(II) complexes bearing a bulky N-heterocyclic carbene for catalysis of Kumada-Tamao-Corriu cross-coupling reactions of aryl halides, Eur. J. Inorg. Chem. (2012) 3079–3086, https://doi.org/10.1002/ejic.201200095.

[49] J. Mao, F. Liu, M. Wang, L. Wu, B. Zheng, S. Liu, J. Zhong, Q. Bian, P.J. Walsh, Cobalt-bisoxazoline-catalyzed asymmetric kumada cross-coupling of racemic α-bromo esters with aryl grignard reagents, J. Am. Chem. Soc. 136 (2014) 17662–17668, https://doi.org/10.1021/ja5109084.

[50] A. Mukherjee, D. Milstein, Homogeneous catalysis by cobalt and manganese pincer complexes, ACS Catal. 8 (2018) 11435–11469, https://doi.org/10.1021/acscatal.8b02869.

[51] M. Uemura, R. Miyake, H. Nishimura, Y. Matsumoto, T. Hayashi, New chiral phosphine ligands containing ($\eta^6$-arene)chromium and catalytic asymmetric cross-coupling reactions, Tetrahedron: Asymmetry 3 (1992) 213–216, https://doi.org/10.1016/S0957-4166(00)80193-7.

[52] S.B. Rana, Influence of CTAB assisted capping on the structural and optical properties of ZnO nanoparticles, J. Mater. Sci. Mater. Electron. 28 (2017) 13787–13796, https://doi.org/10.1007/s10854-017-7224-8.

[53] R.A. Ismail, H.A. Rawdhan, D.S. Ahmed, High-responsivity hybrid α-$Ag_2S$/Si photodetector prepared by pulsed laser ablation in liquid, Beilstein J. Nanotechnol. 11 (2020) 1596–1607, https://doi.org/10.3762/bjnano.11.142.

[54] D. Deep Yadav, R. Jha, S. Singh, A. Kumar, Synthesis and characterisation of Nickel oxide nanoparticles using CTAB as capping agent, Mater. Today Proc. 73 (2023) 333–336, https://doi.org/10.1016/j.matpr.2022.11.012.

[55] M.I.D. Mardjan, M.F. Hariadi, I.M. Putri, N.A. Musyarrofah, M. Salimah, P. Priatmoko, B. Purwono, L. Commeiras, Ultrasonic-assisted-synthesis of isoindolin-1-one derivatives, RSC Adv. (2022) 19016–19021, https://doi.org/10.1039/d2ra02720h.

[56] R.F. Martínez, G. Cravotto, P. Cintas, Organic sonochemistry: a chemist's timely perspective on mechanisms and reactivity, J. Org. Chem. 86 (2021) 13833–13856, https://doi.org/10.1021/acs.joc.1c00805.

[57] I.V. Machado, J.R.N. dos Santos, M.A.P. Januario, A.G. Corrêa, Greener organic synthetic methods: sonochemistry and heterogeneous catalysis promoted multicomponent reactions, Ultrason. Sonochem. 78 (2021) 1–48, https://doi.org/10.1016/j.ultsonch.2021.105704.

[58] L. Rahimi, Y. Mansoori, A. Nuri, B. Koohi-Zargar, D. Esquivel, A new Pd(II)-supported catalyst on magnetic SBA-15 for C-C bond formation via the Heck and Hiyama cross-coupling reactions, Appl. Organomet. Chem. 35 (2021) 1–18, https://doi.org/10.1002/aoc.6078.

[59] M. Yousaf, A.F. Zahoor, R. Akhtar, M. Ahmad, S. Naheed, Development of green methodologies for Heck, chan–lam, Stille and suzuki cross-coupling reactions, Mol. Divers. 24 (2020) 821–839, https://doi.org/10.1007/s11030-019-09988-7.

[60] H. Veisi, Z. Joshani, B. Karmakar, T. Tamoradi, M.M. Heravi, J. Gholami, Ultrasound assisted synthesis of Pd NPs decorated chitosan-starch functionalized $Fe_3O_4$ nanocomposite catalyst towards Suzuki-Miyaura coupling and reduction of 4-nitrophenol, Int. J. Biol. Macromol. 172 (2021) 104–113, https://doi.org/10.1016/j.ijbiomac.2021.01.040.

[61] T. Baran, Ultrasound-accelerated synthesis of biphenyl compounds using novel Pd(0) nanoparticles immobilized on bio-composite, Ultrason. Sonochem. 45 (2018) 231–237, https://doi.org/10.1016/j.ultsonch.2018.03.017.

[62] H. Veisi, M. Ghorbani, S. Hemmati, Sonochemical in situ immobilization of Pd nanoparticles on green tea extract coated $Fe_3O_4$ nanoparticles: an efficient and magnetically recyclable nanocatalyst for synthesis of biphenyl compounds under ultrasound irradiations, Mater. Sci. Eng. C 98 (2019) 584–593, https://doi.org/10.1016/j.msec.2019.01.009.

[63] S.V. Sancheti, P.R. Gogate, Intensification of heterogeneously catalyzed Suzuki-Miyaura cross-coupling reaction using ultrasound: understanding effect of operating parameters, Ultrason. Sonochem. 40 (2018) 30–39, https://doi.org/10.1016/j.ultsonch.2017.01.037.

[64] C. Han, R. Qi, R. Sun, K. Fan, B. Johannessen, D.C. Qi, S. Cao, J. Xu, Enhanced support effects in single-atom copper-incorporated carbon nitride for photocatalytic suzuki cross-coupling reactions, Appl. Catal., B 320 (2023) 1–9, https://doi.org/10.1016/j.apcatb.2022.121954.

[65] A.P. Dysin, A.R. Egorov, O. Khubiev, R. Golubev, A.A. Kirichuk, V.N. Khrustalev, N.N. Lobanov, V.V. Rubanik, A.G. Tskhovrebov, A.S. Kritchenkov, Novel highly efficient green and reusable Cu(II)/Chitosan-Based catalysts for the Sonogashira, buchwald, aldol, and dipolar cycloaddition reactions, Catalysts 13 (2023) 1–26, https://doi.org/10.3390/catal13010203.

[66] S. Iraqui, B. Kalita, R. Star, M. Gupta, M.H. Rashid, Green synthesis of shape-tunable $CuFe_2O_4$ NPs: a magnetically retrievable and efficient catalyst for Chan-Lam type C-N coupling reactions under base-free conditions, New J. Chem. 47 (2023) 10564–10575, https://doi.org/10.1039/d3nj00733b.

[67] B. Ekka, G. Dhar, S. Sahu, M. Mishra, P. Dash, R.K. Patel, Removal of Cr(VI) by silica-titania core-shell nanocomposites: in vivo toxicity assessment of the adsorbent by Drosophila melanogaster, Ceram. Int. 47 (2021) 19079–19089, https://doi.org/10.1016/j.ceramint.2021.03.254.

[68] L. Efiyanti, W. Trisunaryanti, S. Bahri, Y.L. Ni'mah, N.M. Wulandari, S.D. Sumbogo, Synthesis of mesoporous silica from beach sand using variation of cetyl trimethyl ammonium bromide (CTAB), Proc. 3rd KOBI Congr. Int. Natl. Conf. 14 (2021) 374–381, https://doi.org/10.2991/absr.k.210621.063.

[69] H. Purwaningsih, Y. Ervianto, V.M. Pratiwi, D. Susanti, A. Purniawan, Effect of cetyl trimethyl ammonium bromide as template of mesoporous silica MCM-41 from rice husk by sol-gel method, IOP Conf. Ser. Mater. Sci. Eng. 515 (2019) 1–9, https://doi.org/10.1088/1757-899X/515/1/012051.

[70] N.M. Wulandari, L. Efiyanti, W. Trisunaryanti, H.S. Oktaviano, S. Bahri, Y. Lailun Ni'mah, S. Larasati, Effect of CTAB ratio to the characters of mesoporous silica prepared from rice husk ash in the pyrolysis of α–cellulose, Bull. Chem. React. Eng. Catal. 16 (2021) 632–640, https://doi.org/10.9767/BCREC.16.3.10828.632-640.

[71] L. Usgodaarachchi, C. Thambiliyagodage, R. Wijesekera, M.G. Bakker, Synthesis of mesoporous silica nanoparticles derived from rice husk and surface-controlled amine functionalization for efficient adsorption of methylene blue from aqueous solution, Curr. Res. Green Sustain. Chem. 4 (2021) 1–11, https://doi.org/10.1016/j.crgsc.2021.100116.

[72] L. Wang, K. Zhang, Z. Hu, W. Duan, F. Cheng, J. Chen, Porous CuO nanowires as the anode of rechargeable Na-ion batteries, Nano Res. 7 (2014) 199–208, https://doi.org/10.1007/s12274-013-0387-6.

[73] D.S. Zimbovskiy, A.I. Gavrilov, B.R. Churagulov, Synthesis of copper oxides films via anodic oxidation of copper foil followed by thermal reduction, IOP Conf. Ser. Mater. Sci. Eng. 347 (2018) 1–8, https://doi.org/10.1088/1757-899X/347/1/012010.

[74] D.C.L. Vasconcelos, V.C. Costa, E.H.M. Nunes, A.C.S. Sabioni, M. Gasparon, W.L. Vasconcelos, Infrared spectroscopy of titania sol-gel coatings on 316L stainless steel, Mater. Sci. Appl. 2 (2011) 1375–1382, https://doi.org/10.4236/msa.2011.210186.

[75] G.F. Andrade, G. da S. Lima, P.L. Gastelois, D. Assis Gomes, W.A. de A. Macedo, E.M.B. de Sousa, Surface modification and biological evaluation of kojic acid/silica nanoparticles as platforms for biomedical systems, Int. J. Appl. Ceram. Technol. 17 (2020) 380–391, https://doi.org/10.1111/ijac.13376.

[76] J. Wang, Q. Ran, X. Xu, B. Zhu, W. Zhang, Preparation and optical properties of $TiO_2$-$SiO_2$ thin films by sol-gel dipping method, IOP Conf. Ser. Earth Environ. Sci. 310 (2019) 2–7, https://doi.org/10.1088/1755-1315/310/4/042029.

[77] U. Anggarini, L. Yu, H. Nagasawa, M. Kanezashi, T. Tsuru, Metal-induced aminosilica rigidity improves highly permeable microporous membranes via different types of pendant precursors, ACS Appl. Mater. Interfaces 14 (2022) 42692–42704, https://doi.org/10.1021/acsami.2c11588.
[78] X. Fan, J. Yang, Q. Pang, Z. Liu, P. Zhang, J.H. Yang, Ultrafine and highly dispersed Pd/$SiO_2$ for Suzuki−Miyaura cross-coupling reactions, Catal. Lett. 151 (2021) 2291–2301, https://doi.org/10.1007/s10562-020-03465-9.
[79] C.A. Busacca, D.R. Fandrick, J.J. Song, C.H. Senanayake, Applications of Transition Metal Catalysis in Drug Discovery and Development: an Industrial Perspective, John Wiley & Sons, Inc., New Jersey, 2012, https://doi.org/10.1002/9781118309872.ch1.
[80] P. Mondal, P. Bhanja, R. Khatun, A. Bhaumik, D. Das, S. Manirul Islam, Palladium nanoparticles embedded on mesoporous $TiO_2$ material (Pd@M$TiO_2$) as an efficient heterogeneous catalyst for Suzuki-Coupling reactions in water medium, J. Colloid Interface Sci. 508 (2017) 378–386, https://doi.org/10.1016/j.jcis.2017.08.046.
[81] A. Ohtaka, Recent progress of metal nanoparticle catalysts for C–C bond forming reactions, Catalysts 11 (2021) 1–35, https://doi.org/10.3390/catal11111266.
[82] S. Rana, G. Bishwa Bidita Varadwaj, S.B. Jonnalagadda, Ni nanoparticle supported reduced graphene oxide as a highly active and durable heterogeneous material for coupling reactions, Nanoscale Adv. 1 (2019) 1527–1530, https://doi.org/10.1039/c8na00245b.
[83] P. Styring, C. Grindon, C.M. Fisher, A polymer-supported nickel(II) catalyst for room temperature Tamao-Kumada-Corriu coupling reactions, Catal. Lett. 77 (2001) 219–225, https://doi.org/10.1023/A:1013209202418.
[84] R.G. Singh, G.D. Yadav, Synthesis of biphenyl via sustainable Suzuki-Miyaura coupling reaction using mesoporous MCF-supported tin-palladium nanoparticles, Mol. Catal. 553 (2024) 1–17, https://doi.org/10.1016/j.mcat.2023.113747.
[85] P.S. Pharande, G.S. Rashinkar, D.M. Pore, Cellulose Schiff base-supported Pd(II): an efficient heterogeneous catalyst for Suzuki Miyaura cross-coupling, Res. Chem. Intermed. 47 (2021) 4457–4476, https://doi.org/10.1007/s11164-021-04528-1.
[86] H. Tang, M. Yang, X. Li, M.L. Zhou, Y.S. Bao, X.Y. Cui, K. Zhao, Y.Y. Zhang, Z.B. Han, Synthesis of biaryl compounds via Suzuki homocoupling reactions catalyzed by metal organic frameworks encapsulated with palladium nanoparticles, Inorg. Chem. Commun. 123 (2021) 1–7, https://doi.org/10.1016/j.inoche.2020.108368.
[87] A. Zarnegaryan, D. Elhamifar, An efficient and heterogeneous Pd-containing modified graphene oxide catalyst for preparation of biaryl compounds, Heliyon 6 (2020) e03741, https://doi.org/10.1016/j.heliyon.2020.e03741.
[88] H.H. Moghadam, S. Sobhani, J.M. Sansano, New nanomagnetic heterogeneous cobalt catalyst for the synthesis of aryl nitriles and biaryls, ACS Omega 5 (2020) 18619–18627, https://doi.org/10.1021/acsomega.0c01002.
[89] Y. Rangraz, F. Nemati, A. Elhampour, A novel magnetically recoverable palladium nanocatalyst containing organoselenium ligand for the synthesis of biaryls via Suzuki-Miyaura coupling reaction, J. Phys. Chem. Solid. 138 (2020), https://doi.org/10.1016/j.jpcs.2019.109251.